Earth Moon Planets (2015) 114:101–135
DOI 10.1007/s11038-015-9459-9

Improved Views of the Moon in the Early Twenty First Century: A Review

Hongwei Yang · Wenjin Zhao

Received: 23 October 2014 / Accepted: 10 January 2015 / Published online: 20 January 2015

Abstract The twenty first century was an exciting epoch in planetary exploration, when a large number of lunar scientific achievements were accomplished. New missions in the first decade of the twenty first century have herald a new and exciting phase in lunar exploration, including *LRO*, *LCROSS*, the dual *GRAIL* orbiters, *Kaguya*, *Chandrayaan 1*, and the *Chang'e* series. Here we review the most significant advances in our understanding of lunar geoscience, including the assessment of water ice at lunar poles, the detection of new elements and minerals relating to exposed interior materials, the calculation of highly accurate gravity models, and the detection of subsurface interfaces probably related to basaltic strata formed in distinct episodes. In this paper we emphasize the importance of integrated approaches to the analysis of these large yield of new lunar data, through comparison and integration. By integrating a range of diverse technologies and approaches, this paper reviews new understanding of lunar processes, including the confirmation of the presence of water ice at the poles, the interactions between solar wind and surface oxides, and an improved model of lunar interior structures.

Keywords Moon · Lunar explorations in early twenty first century · Lunar geosciences

1 Introduction

In the 1960s, 381.7 kg of lunar materials were returned by the *Apollo* missions and 326 g by the *Luna* missions. These samples were collected to provide true constraints in a geological context for future research of the Moon. In the 1990s, the *Clementine* and *Lunar Prospector* spacecraft acquired remote sensing data and gravity observations covering most of the Moon. Our understanding of the lunar evolution were reconsidered through an integrated analysis of the remote data along with the samples returned, and new models of the lunar magma ocean

H. Yang (✉) · W. Zhao
Chinese Academy of Geological Sciences, No. 26 Baiwanzhuang Road, Beijing 100037, China
e-mail: yhw1106@163.com

and identification of KREEP rocks were constructed. The new findings were reviewed and summarized in 'New Views of the Moon' (Jolliff et al. 2006) and its Chinese version (Jolliff et al. 2012). Because of the limitations in technology, methodology, and understanding of the Moon, there remained numerous issues worthy of future investigation. Nine key questions for lunar science were proposed by Jolliff et al. (2006, 2012): (1) the structure and evolution of the lunar crust; (2) the composition and structure of the lunar mantle; (3) the extent of the lunar magma ocean; (4) the relationship between the surface materials and interior structure and evolution; (5) the nature of the Moon's asymmetry; (6) the origin, evolution, and distribution of mare volcamism (7) the timing and effects of the major basin-forming impacts on lunar crustal stratigraphy, especially the South Pole-Aitken Basin; (8) the origin of lunar paleomagnetism; (9) the Moon's important resources. Moreover, Jaumann et al. (2012) summarized the improvements in lunar science understanding from recent missions as supplemental materials for 'New Views of the Moon'. Some chapters (23–25) in the book 'The Encyclopedia of the Solar System' (Hiesinger and Jaumann 2014; Crawford et al. 2014; Weber 2014) summarized all missions and payloads throughout the whole lunar history until now, and their highlights of key scientific knowledge and lunar scientific questions to be addressed in future.

There are four noticeable features in this paper that contrast with these reviews. (1) In this paper, comparisons between diverse types of observations derived from the missions in early twenty first century give rise to identification and choice of the data sets. (2) The significance of integration of approaches and data sets to the lunar science researches is pointed out and emphasized here. (3) The key role of integration of approaches and the variety of data sets in determining what strategies will be the best ways for specific problem of lunar science researches is proposed and discussed in detail in this paper. (4) Some new understanding and models are established through the integration procedures.

The first decade of the twenty first century has been another exciting period in lunar exploration. New knowledge have been added by a series of recent lunar explorations, including the Japanese *Kaguya* mission (also known as SELENE; 2008), the Indian *Chandrayaan 1* (2008), the U.S. *Lunar Reconnaisance Orbiter* (*LRO*; 2009), *Lunar Crater Observation and Sensing Satellite* (*LCROSS*; 2009), and *Gravity Recovery and Interior Laboratory* (*GRAIL*; 2012), and Chinese *Chang'e 1* (2007) and *Chang'e 2* (2010). Compared with earlier missions, the technologies and approaches applied were sufficiently developed that greatly improved remote sensing data were obtained and the gravitational field could be constructed with unprecedented accuracy, all of which helped promote developments in lunar science.

The most significant achievements in technology, methodology, and our understanding of lunar science during this period are reviewed in this paper. First, the possibility of the presence of water ice at the lunar poles has been studied through the integration of various remote sensing data sets (Sect. 2), including establishing the illumination conditions with digital elevation models from the instruments LALT (*Kaguya*) and LOLA (*LRO*), the concentration of hydrogen and hydroxyl by LEND (*LRO*) and M^3 (*Chandrayaan 1*), respectively, the circular polarization ratio by Mini-SAR (*Chandrayaan 1*) and Mini-RF (*LRO*), the temperature conditions by Diviner (*LRO*), and the volatile content of the Cabeus crater debris plume by *LCROSS*. In Sect. 3, we discuss the distributions of new elements and minerals relating to the interior composition and evolution of the Moon, which were first observed and established with new data from the GRS, Spectral Profiler, and Multiband Imager on *Kaguya*, M^3 on *Chandrayaan 1*, and Diviner on *LRO*. Moreover, large gaps in the orbital data over the lunar far side were filled by *Kaguya* and *GRAIL* data, allowing the calculation of the first global gravity field of the Moon with unprecedented accuracy: this and the resultant deductions about mascons and interior structures are

discussed in Sect. 4. Finally, the detections by the *Kaguya* LRS of subsurface strata, probably related to the distribution of basaltic units, are summarized in Sect. 5.

2 Detection of Water Ice at the Lunar Poles

Confirming the possibility of the presence of water ice on the Moon has scientific importance and is of great practical significance for the possibility of human survival on the Moon. To establish a lunar base, favorable locations will be those with water resources that can provide not only life supply but energy. The lunar poles are the best location candidates. In the early history of lunar exploration, samples returned by the *Apollo* missions revealed that volatile elements are depleted on the Moon (Heiken et al. 1991). However, remote sensing data from *Clementine* and the *Lunar Prospector* provided some indirect evidence of the possible presence of water ice in permanently shadowed areas (PSRs) at both lunar poles: in 1994, polar PSRs were first detected by observations from the ultraviolet/visible camera on board *Clementine*, but observations by the Bistatic Radar Experiment in the same mission to determine the presence of water ice deposits remained contentious, because of the irreproducibility of their own (discussed in Sect. 2.4) (Nozette et al. 1996; Campbell et al. 2006). After several years, measurements from the epithermal and fast-neutron spectrometers on the *Lunar Prospector* confirmed the hydrogen content of the polar deposits. These results demonstrated that measuring the epithermal neutron flux was 10 times more effective at detecting hydrogen in lunar regolith than the fast neutron flux, but the existence of water ice remained unconfirmed, because the epithermal neutron flux is affected not only by the content of water ice deposited, but also by the extent of the PSRs (Feldman et al. 1998). Therefore, the extent of the PSRs had to be quantified by subsequent missions. Moreover, the possibility of water ice at the lunar poles required confirmation from higher accuracy data from epithermal neutron fluxes and other remote sensing data.

From the beginning of this century, many refined instruments, approaches and multidisciplinary analyses of recent missions supported the existence of water ice and approximately quantified its extent. The illumination conditions and extent of PSRs at the lunar poles were determined with digital elevation models using LALT and LOLA data from the *Kaguya* and *LRO* missions, respectively (Sect. 2.1). The polar distribution of hydrogen at higher spatial resolution was established by LEND on *LRO* (Sect. 2.2). Hydroxyl-bearing materials at the poles detected by the M^3 instrument on board *Chandrayaan 1* provided additional clues to water ice (Sect. 2.3). Following on *Clementine*, new polarimetric data were acquired by synthetic aperture radar sensors, including Mini-SAR and Mini-RF on board *Chandrayaan 1* and *LRO*, respectively (Sect. 2.4). In addition, temperature conditions sufficient to preserve water ice were established by Diviner on *LRO* (Sect. 2.5). Finally, the abundance of water ice in the ejecta plume from the Cabeus crater, a PSR at the lunar south pole, was detected and quantified by *LCROSS* and *LRO* (Sect. 2.6). Comparative analyses and integrated approaches confirmed the possibility of the presence of water ice from varied aspects and produced new knowledge (Sect. 2.7).

2.1 Illumination Conditions

Determination of the illumination conditions at the lunar poles can provide essential information not only for choosing candidate lunar base sites but also for locating water ice. Because of the inclination of 1.5° to the lunar spin axis (Ward 1975) and complex topography at the poles, some regions there, for example, at higher altitudes such as lunar

ridges and rims of some craters, are the most likely to be well illuminated for a longer time per lunar year, but other areas at lower altitude and in shadow, such as walls of craters, will be dark most of the year. In addition, because of the Moon's practically non-existing atmosphere, the surface temperature is directly susceptible to sunlight. In some equatorial regions, the highest temperature exceeds 390 K and the lowest 110 K (Heiken et al. 1991). The shadowed areas at the lunar poles also create cold traps, with some regions having lowest temperatures of 40 K (Bussey et al. 2001), enough to preserve water ice.

So far, there have been two approaches to determine the illumination conditions at the lunar poles. One is based on photographic imagery, and the other employs digital elevation models (DEMs) constructed from Earth-based radar, laser altimeters, or both. The mosaic photographic images produced from the *Clementine* Ultraviolet/Visible Camera (UVVIS) data were first applied to produce illumination maps of the south pole above 85°S (Bussey et al. 1999) and the north pole above 75°N (Bussey et al. 2005) at a resolution of 500 m/pixel. Nonetheless, the UVVIS data, which were acquired just after midwinter in the southern hemisphere, were insufficient to calculate the average changes in illumination over a year or even over multiple years. New polar images with a resolution of 0.5 m (Vondrak et al. 2010) from the Lunar Reconnaissance Orbiter Camera (LROC) were able to provide more detailed illumination maps. Although this method requires as many satellite photographic images at different periods as possible to reliably evaluate yearly illumination conditions, these observations detected over years are still not adequate but can still be employed as realistic images to validate DEM-based methods, as described below.

Alternatively, the illumination conditions can be estimated by integrating high-accuracy DEMs and sunlight conditions from lunar ephemeris files. The earliest DEMs used to evaluate the sunlit conditions of the lunar poles were produced by the Earth-based Goldstone Solar System Radar (GSSR) interferometer. The first group of DEMs for both polar regions above 85° on the nearside, with spatial and vertical resolutions of 150 and 50 m, respectively, were created in 1999 using the GSSR radar observations (Margot et al. 1999), and the second group, with 40 and 5 m resolution, in 2010, which was also used to estimate the average conditions over the years 2009–2028 (Bryant 2010). By contrast, Earth-based radar imaging is constrained to areas over the near side of the Moon and small parts of the farside because of polar motion in which the radar's line of sight cannot be blocked by complex terrain.

An alternative technique to construct DEMs relies on observations from laser altimeters. The first such DEMs, with resolution of 470 m, for $\sim$85° at the lunar poles were generated by observations from LALT on board *Kaguya* (Araki et al. 2009a, b). The resolution of this model, which was compared with the mosaic images from *Clementine*, proved to be enough to make a reliable assessment of the polar illumination conditions. With these detailed topographic models, Bussey et al. (2010) calculated average illumination seasonal variations through 2020, and Noda et al. (2008) constructed the average for the coming 2,000 days (about 5.5 years). In the following years, more accurate topographical models were built with new altimetry data from the Lunar Orbiter Laser Altimeter (LOLA) on board *LRO* (Smith et al. 2010). Mazarico et al. (2011) afterward produced polar DEMs for $\sim$75° with 240 m/pixel resolution and evaluated the average lighting conditions for the longest time span, from 1970 to 2044, which includes about four lunar precessions. These results had also been compared with higher resolution mosaic images at 0.5 m from the LROC wide-angle camera (Vondrak et al. 2010). Comparison of DEMs from Earth-based radar and orbital laser altimeters demonstrates that, in future missions, higher resolution data sets will be provided by onboard radar interferometers rather than laser altimeters, and

by combing different DEM-based models with photographic images. Evaluating the illumination conditions over the history of the Moon from the variation of polar motion including precession nutation remains a major problem (Siegler et al. 2011).

High-resolution polar DEMs produced by Noda et al. (2008) and Bussey et al. (2010) with LALT data and by Mazarico et al. (2011) with LOLA indicated that there were no continuously illuminated regions but that there were permanently shadowed regions (PSRs). Furthermore, the existence of these shadowed areas was also supported by observations from the Earth-based GSSR (Margot et al. 1999; Bryant 2010). Most of the areas with similar average illumination are reported in these papers. In the LALT-based simulations by Noda et al. and Bussey et al. the north pole site with the highest sunlight exposure, 89 %, is located at (88.1°N, 117.6°W) and that at the south pole, with 86 %, is located at (88.8°S, 124.5°E); by contrast, the LOLA-based simulation by Mazarico et al. found peaks of 86 % for the north pole at (88.06°N, 242.24°E) and 89 % for the south pole

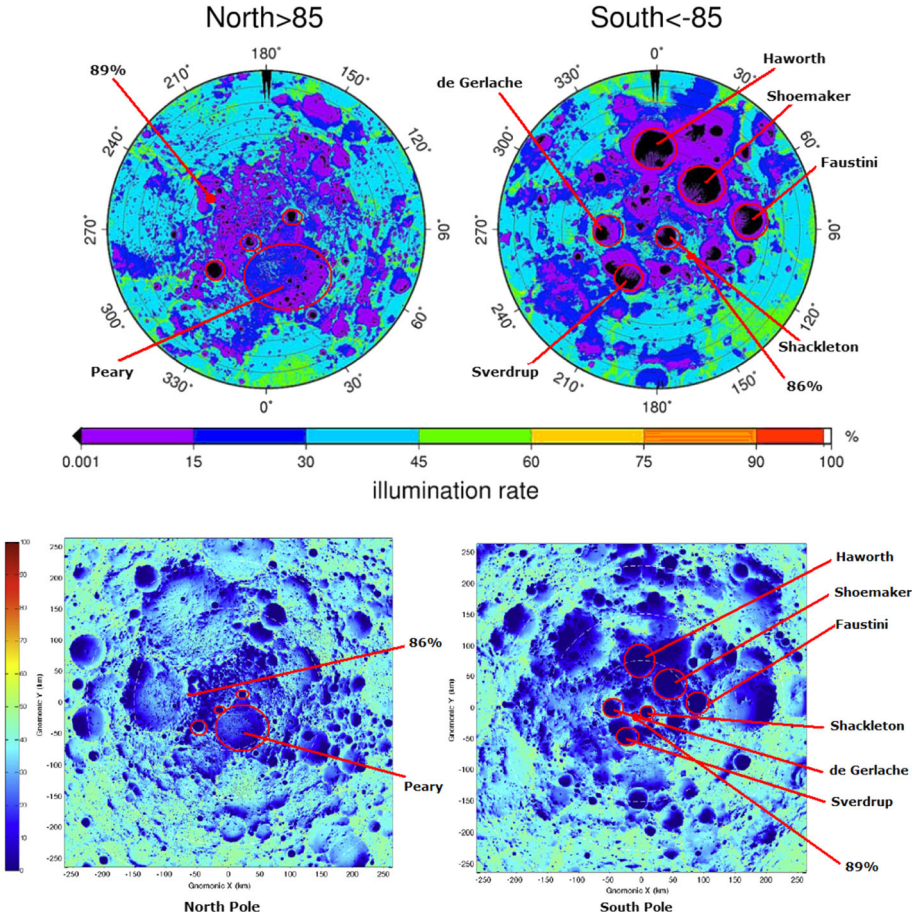

Fig. 1 Maps of illumination percentage at both lunar poles (*dark blue areas*, PSRs; *red spots*, sites with the highest illumination) The *top* panels are reproduced and used by permission of John Wiley and Sons Inc., after Noda et al. (2008), Fig. 3, and the *bottom* panels reproduced and used by permission of Elsevier Publisher after Mazarico et al. (2011), Fig. 6. (Color figure online)

at (89.45°S, 222.69°E) (see Fig. 1). These discrepancies probably arise from the duration of the illumination conditions evaluated and the accuracy of the data sets. At the other extreme, the largest permanently shadowed craters at the south pole (Fig. 1) include Haworth (86.5°S, 0.0°E), Shoemaker (88.1°S, 44.9°E), Faustini (87.3°S, 77.0°E), Sverdrup (88.5°S, 152.0°W), de Gerlache (88.5°S, 87.1°W), and Shackleton (89.9°S, 0.0°E), and those at the north pole are three much smaller craters at the floor of Peary (88.6°N, 33.0°E). Detailed information about the extent and size of illuminated and shaded regions above different latitudes is provided by Noda et al. (2008) and Mazarico et al. (2011).

2.2 Hydrogen Distribution

The regions characterized by a suppression of epithermal neutrons, referred to as neutron suppression regions (NSRs), are probably associated with regolith with enhanced hydrogen content. Previous observations from the omnidirectional sensor on board the *Lunar Prospector* and the Lunar Exploration Neutron Detector (LEND) on *LRO* were used to produce maps of epithermal neutral flux at spatial resolutions of 44 km (Maurice et al. 2004) and 60 km (Litvak et al. 2012), which are larger than most PSRs. New maps (Fig. 2) at the lunar poles with advanced spatial resolution of 10 km from the LEND collimated sensor made possible an analysis of the correlation of the distributions of NSRs, PSRs, and temperature (Mitrofanov et al. 2012; Sanin et al. 2012). These improved results indicate that there is no direct correlation between NSRs and PSRs. Suppression regions were found both inside and outside of PSRs, while some PSRs appear to show an excess of epithermal neutron emission. For example, a comparison of Fig. 1 with Fig. 2 reveals that some areas with strong suppression of neutron flux are located both at PSRs (Fig. 1, *dark blue*) and their outside, while a few small-scale shadowed areas (*red circles in* Fig. 2) have large excess flux. Understanding the reasons for these differences in distribution and their origin will require improved knowledge of the physical properties of the hydrogen-rich

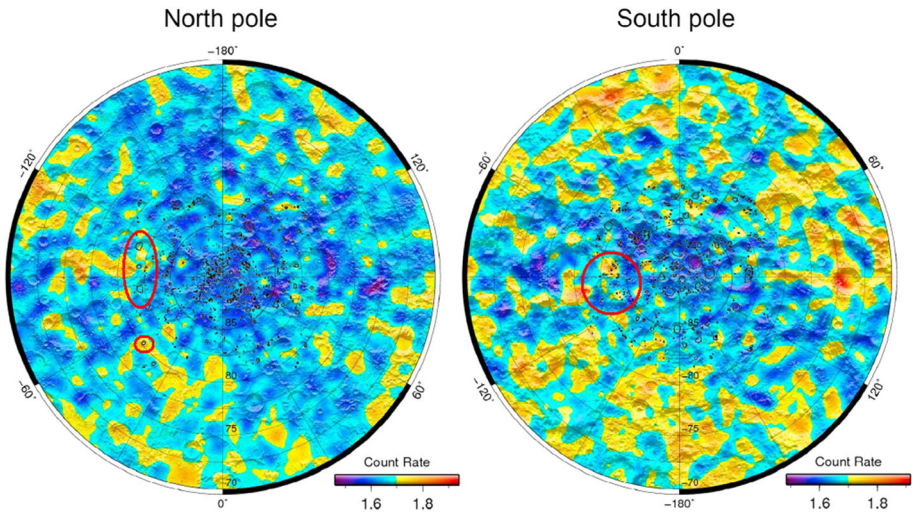

Fig. 2 Maps (10 km spatial resolution) of epithermal neutron count rates above 70° latitude at the lunar north (*left*) and south (*right*) poles [reproduced and used by permission of John Wiley and Sons Inc., after Mitrofanov et al. (2012), Fig. 1]. (Color figure online)

permafrost on the lunar surface or higher resolution maps of the PSRs' extent. The limited depth (<100 cm) of neutron spectrometers is another obstacle to uncovering the origin of the water ice at the lunar poles.

2.3 Hydroxyl Distribution

The NASA-designed Moon Mineralogy Mapper (M^3) on board *Chandrayaan 1* detected an absorption peak near 2.8–3.0 μm, suggestive of the presence of hydroxyl- and/or water ice–bearing phases on the surface at the lunar poles (Pieters et al. 2009). These absorption features are consistent with results from the Visual and Infrared Mapping Spectrometer aboard the earlier flyby spacecraft *Cassini* (Clark 2009) and from *Deep Impact* (Sunshine et al. 2009). Although M^3 provided the highest spatial resolution at 140 m/pixel, its spectral range, from 430 to 3,000 nm, compared with the coverage from 350 to 5,000 nm of *Cassini* and from 1050 nm to 4500 of *Deep Impact*, limited its ability to reveal the full shape of the hydration features from 2.8 to 3.6 μm (Fig. 3). The amount of water at the north pole was estimated to be 10–1000 ppm from the *Cassini* results, 770 ppm from M^3, and less than 5,000 ppm from *Deep Impact*. On the other hand, there are large inconsistencies in the hydroxyl distributions derived from these observations compared with those of hydrogen from the *Lunar Prospector* and *LRO*. First, the depth to which the top surface of the lunar soil could be investigated by M^3 and the Lunar Prospector Neutron Spectrometer (LP-NS) was different. Moreover, the absorption features near 3 μm due to O–H or H–O–H bonds can be clearly identified only at very high signal-to-noise ratio. This was constrained by incomplete removal of thermal emission effects from the M^3 observations because of the limited spatial and temporal coverage (McCord et al. 2011). Similarly, uncertainty about the form of hydrogen (water or hydroxyl) represents another difficulty. The distribution and abundance of hydration phases (involving water ice or hydrated mineral phases) is not easy to ascertain just from the detection of hydroxyl and hydrogen without a sound understanding of the nature of their physical properties. Comparative research based on additional evidence and knowledge will likely aid further understanding of the distribution of water ice at the lunar poles (see Sect. 2.7 for a more detailed discussion).

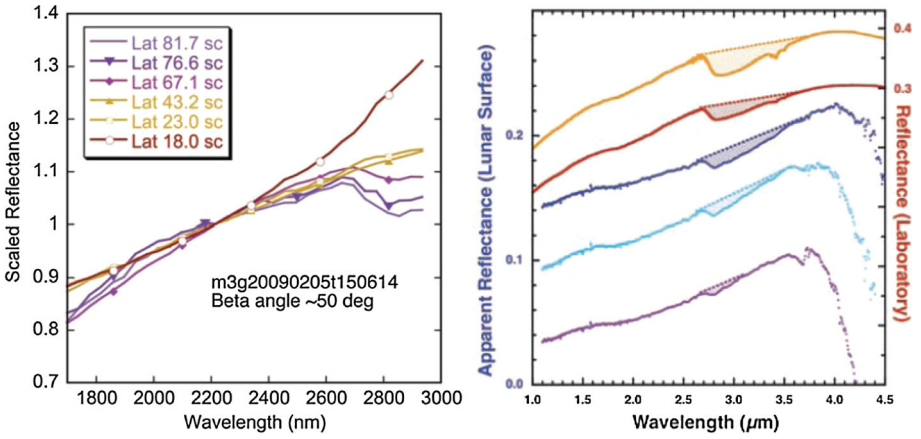

Fig. 3 Partial (*left*) and full (*right*) spectra of the absorption features near 3,000 nm [used by permission of American Association for the Advancement of Science, after Pieters et al. (2009), Fig. 3 and after Sunshine et al. (2009), Fig. 1). (Color figure online)

2.4 Circular Polarization Ratio

Debates had gone on for a decade whether a high circular polarization ratio (CPR, the ratio of the power of the reflected signal in the same circular polarization sense to that of the transmitted signal with the opposite sense) could provide evidence for the presence of water ice at the lunar poles. The elevated CPR at the lunar south pole initially detected by the *Clementine* Bistatic Radar Experiment was explained by Nozette et al. (1996) as indicative of a low transmission loss object, such as ice. This interpretation was questioned by Stacy et al. (1997), Margot et al. (1999), and Campbell et al. (2006) on the basis of Earth-based radar measurements from the Arecibo radio telescope, Goldstone Solar System Radar (GSSR) interferometer and Robert C. Byrd Green Band Telescope with similar wavelength and areas to those of *Clementine*. They suggested instead that surface roughness could explain the high CPR and that roughness other than the existence of water ice (in the areas no greater than 1 km^2) accounted for the anomalies in observations. Furthermore, the high-CPR result from *Clementine* was controversial because it was observed only in orbit 234, which included both the PSRs and sunlit areas (Nozette et al. 1997; Stacy et al. 1997; Nozette et al. 2001; Campbell et al. 2006). Nozette et al. (1996) demonstrated that the enhanced CPR from *Clementine* could have been observed only under conditions in which the bistatic angle or phase was very close to zero at the same time the coherent backscatter opposition effect (Hapke 1990) would occur. These conditions could not be reproduced at all by Earth-based stationary radar systems because of the difficulties in realizing the particular geometry between the satellite as transmitter, the Moon as target, and Earth as receiver (Nozette et al. 1997). However, the same conclusion had not been reproduced based on a new approach to analysis of *Clementine* bistatic radar data by Simpson and Tyler (1999). Later studies by Nozette et al. (2001) suggested again that those PSRs with enhanced CPR in newly processed *Clementine* data sets could be indicative of water ice. Furthermore, synthetic aperture radar observations with the optimum incidence angle of 45° were also suggested for future mission by Nozette et al. (2001) and Spudis et al. (2009).

It was not until 2009 that new polarimetric data acquired by a synthetic aperture radar, Mini-SAR on *Chandrayaan 1*, at the optimum incidence angle of around 45°, had the ability to distinguish between high CPR attributed to surface roughness and to low-loss material such as water ice (Spudis et al. 2010). Using a similar principle, the *LRO* Mini-RF produced CPR mosaic images of the lunar poles above 70° with a spatial resolution of 15 m/pixel (Spudis et al. 2013). Careful analysis of both observations suggested that high CPRs at the lunar poles that occurred both inside and outside of craters [such as Main-L (81.7°N, 23.2°E) and Giordano Bruno (35.9°N, 102.8°E)] could be related to rough surfaces with fresh crater deposits and those found only in the interiors could be indicative of water ice deposits [such as Peary (88.6°N, 33°E0 and Hermite (86.0°N, 89.9°W); see Fig. 5]. Similar anomalies in the Shackleton crater (89.6°S, 132.3°E) at the south pole that had previously been suggested to indicate water ice storage by Nozette et al. (2001) were confirmed to be due to surface roughness (Campbell et al. 2006), which was confirmed by a subsequent combined analysis (Zuber et al. 2012). There are 43 "anomalous craters" related to the presence of water ice at the north pole and 28 at the south pole (Table S1 of Spudis 2013). The distributions of these craters is supported by other evidence, including illumination conditions from LALT and LOLA (Fig. 1), neutron fluxes from LP-NS and LEND (Fig. 2), hydroxyl from M^3 (Fig. 4), temperature from Diviner (Fig. 6), and detections of debris from *LCROSS* (Fig. 7).

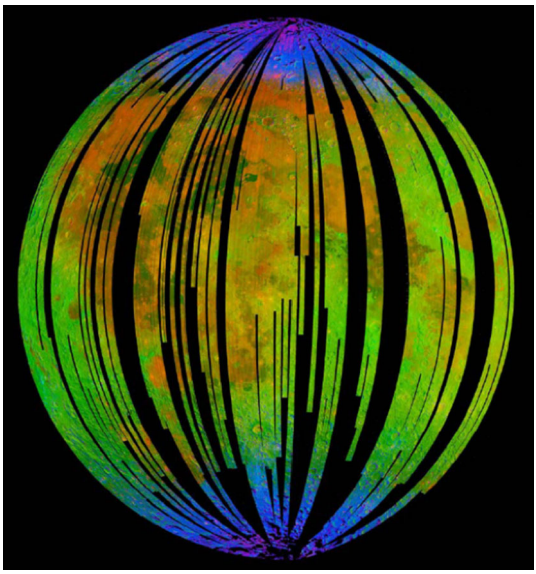

Fig. 4 3,000 nm absorption features due to OH/H_2O. *Dark blue* and *purple* indicate high amounts of hydroxyl- or water-bearing materials [used by permission of American Association for the Advancement of Science, Pieters et al. 2009, Fig. S5). (Color figure online)

2.5 Polar Temperature

Before the final *LCROSS* impact, the daytime surface bolometric brightness temperature at summer solstice in the regions around impact sites at the south pole had been measured by Diviner, with a spatial resolution of 200 m, to be 46.7 K in average (Paige et al. 2010; Fig. 6). The calculated annual average temperature in these regions is about 38 K, extremely cold and adequate to permanently preserve volatiles, including water ice.

2.6 Debris Plume from the Cabeus Crater

Because of its highest content of 470 ppm primarily according to the estimate of hydrogen content measured by LEND (Mitrofanov et al. 2010a), a target (Cabeus SP_C) within the Cabeus crater was chosen from nine candidate sites for the final impact of *LCROSS*. Before that, the corresponding value of water by weight had been estimated to be 0.5 % (Stacy et al. 1997) or 4 % (Hapke 1990; Mitrofanov et al. 2010a) under the assumption either of a single-layer model with uniform hydrogen content with depth or of double layers with overlying dry deposits, respectively. The site with the highest hydrogen content (500 ppm) is located to the east of the chosen impact site (Fig. 7, *inner red contour*). The inconsistency of the distributions between NSRs and PSRs was highlighted again by the detailed contour map of hydrogen content (Fig. 7). Other evidence, such as that the temperature of impact sites derived from Diviner is 60 K, cold enough to preserve water ice, also supports this choice (Paige et al. 2010).

The presence of water in the lunar regolith was confirmed by the detection of water vapor and hydroxyl materials in the ejecta plume by the near-infrared and ultraviolet/visible spectrometers on board *LCROSS*. The total water vapor and water ice were estimated to be 155 ± 12 kg, and the concentration of water by mass in the regolith was 5.6 ± 2.9 % (Colaprete et al. 2010; Dino 2011), which is in good agreement with estimates

Table 1 Relative percentages with respect to H_2O of all debris-plume volatiles detected by *LCROSS* [e.g., for H_2O: 5.1(1.4)E19 = 5.1 ± 1.4 × 10^{19} cm^{-2}; *H_2O(g) is abundance of water vapor] [used by permission of American Association for the Advancement of Science, after Colaprete et al. (2010), Table 2]

Compound	Molecules (cm^{-2})	% Relative to H_2O (g)*
H_2O	5.1(1.4)E19	100.00
H_2S	8.5(0.9)E18	16.75
NH_3	3.1(1.5)E18	6.03
SO_2	1.6(0.4)E18	3.19
C_2H_4	1.6(1.7)E18	3.12
Co_2	1.1(1.0)E18	2.17
CH_3OH	7.8(42)E17	1.55
CH_4	3.3(3.Q)E17	0.65
OH	1.7(0.4)E16	0.03

Table 2 Detailed Information of Moonquake Sources

Type of events	Possible depth (km)	Magnitude	Number of events	Mechanism of origin
Shallow	50–220[a]	5	28	No confirmative results
Deep	700–1,200[b]	3	Over 7,000	Tides by the earth and the sun
Thermal	1.5–4[c]	Small		Temperature variation on surface
Meteoroids		100 g–1,000 kg (mass of meteroids)	1,700	
Artifact	<6[d]		9	

[a] Khan and Mosegaard (2002)

[b] Lammlein et al. (1974)

[c] Duennebier and Sutton (1974)

[d] Kovach et al. (1973)

based on the two-layer model of Mitrofanov et al. (2010a, b). The abundances of other volatile species in the debris plume were determined as well (see Table 1).

2.7 New Ideas Based on Integrated Analyses

Comparative analyses of integrated measurements, including illumination conditions (Figs. 1, 7), the distributions of hydrogen (Figs. 2, 7) and hydroxyl (Fig. 4), CPR (Fig. 5), and bolometric temperature (Figs. 6, 7) have generated new insights regarding and understanding of the presence of lunar water ice.

1. *Presence of water ice* In specific regions with low temperature, elevated CPR, and enhanced abundances of hydrogen and hydroxyl inside PSRs, conditions are suitable to preserve water ice. The water vapor content in the ejecta plume from the Cabeus crater determined by the *LCROSS* mission confirmed the presence of water ice in just such an area. Similar areas with the greatest possibility of harboring water ice include Haworth, Shoemaker, Faustini at the south pole and three small craters in Peary at the north pole (see Figs. 1, 3, 4, 5, 6).

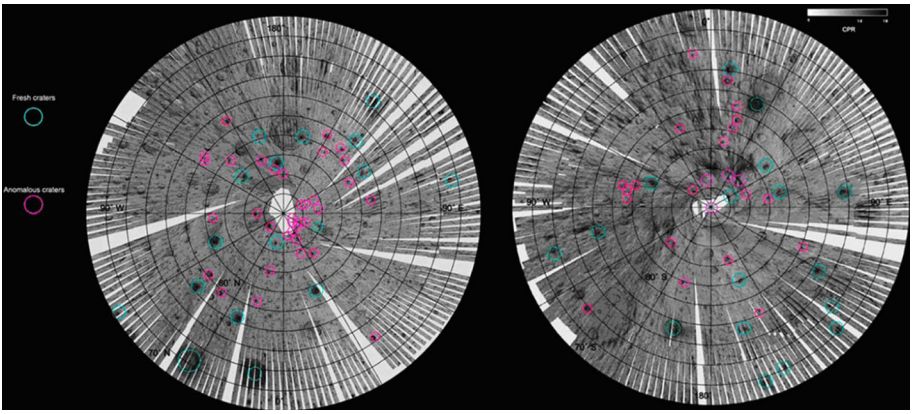

Fig. 5 CPR map of the north (*left*) and south (*right*) lunar poles. *Green circles*, high-CPR craters due to surface roughness; *red circles*, high-CPR areas caused by water ice deposits [reproduced and used by permission of John Wiley and Sons Inc., after Spudis et al. (2013), Fig. 6]. (Color figure online)

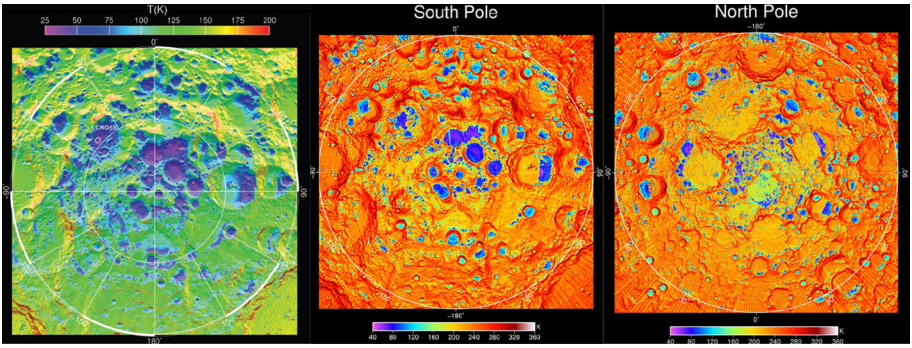

Fig. 6 Diviner-derived daytime bolometric brightness temperature near the *LCROSS* impact site (*left*) [used by permission of American Association for the Advancement of Science, Paige et al. (2010), Fig. 1] and maximum daytime temperature at the south (*middle*) and north (*right*) poles (Diviner: http://diviner.ucla.edu/index.shtml). (Color figure online)

2. *Assessment of current observations* In less consistent regions, the illumination conditions, bolometric temperature, CPR, and hydrogen and hydroxyl content are quite complex, but there is relative agreement regarding the extent of illuminated areas and the distribution of bolometric temperature, although the significant effect of obliquity over the history of the Moon on sunlit conditions should be taken into consideration (Siegler et al. 2011). Because of our lack of knowledge of the hydrogen bonding mode, the relationship of hydrogen and hydroxyl remains complicated. Further measurements from future mission, especially from radar experiments, will aid in the confirmation of the extent of water ice.
3. *Areas with potential water ice preservation* The non-PSR regions beyond 85° latitude have lower average sunlit conditions (Fig. 1) and temperature (Fig. 6), high amounts

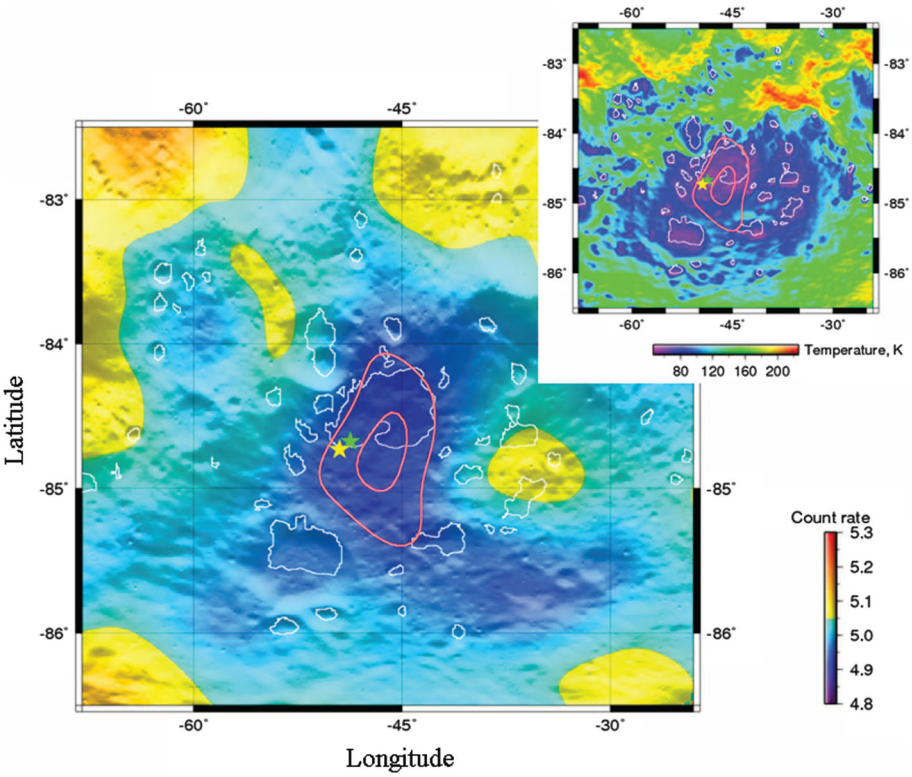

Fig. 7 Epithermal neutron flux (*color scale*), boundaries of the NSR (*red* contours) and the PSRs (*white* contours), the location of the impact sites (*star marks*), and the temperature derived by Diviner (*upper right*) [used by permission of American Association for the Advancement of Science, after Mitrofanov et al. (2010a), Fig. 1]. (Color figure online)

of hydrogen (Fig. 4) and hydroxyl, and elevated CPR (Fig. 5), such as the regions nearby the impact sites in the *LCROSS* mission (Fig. 7). Besides the interpretations by Mitrofanov et al. (2010a), water ice could be also deposited in these areas.

4. *Interactions between solar wind and oxides in lunar surface materials* A comparison between Figs. 1 and 4 demonstrates that enhanced hydrogen abundances also appear in some regions with high illumination. In these regions, the temperature is too high to preserve water ice. Moreover, features higher in hydroxyl but lower in hydrogen (Litvak et al. 2012) were detected in the Goldschmidt crater, which is illuminated for most of the year. These most likely represent the implantation of hydrogen from the solar wind into the subsurface of the lunar regolith and subsequent interaction with some oxides in lunar surface materials, if present, to form hydroxyl-bearing materials. This phenomenon has been validated in laboratory experiments (Burke et al. 2011).

Above all, integrated approaches and comparative analyses confirm the presence of water ice and determine its general extent. However, and importantly, the origin of the water ice at the lunar poles has not yet to be well understood.

3 Detection of New Elements and Minerals on the Lunar Surface

3.1 First Detection of Global Uranium Abundance

Uranium, thorium, and potassium as heat sources of the igneous activity of the Moon are important to understanding its thermal history and origin (Jolliff et al. 2000; Wieczorek and Phillips 2000; Taylor et al. 2006). Before *Kaguya*, the global distribution of uranium had not been measured directly by any spectrometer orbiting the Moon but was instead calculated based on its correlation with the abundance of thorium on the lunar surface. The first reliable uranium distribution map over the whole Moon came from measurements by the *Kaguya* gamma-ray spectrometer (GRS). Because uranium's gamma-ray lines are weak compared with those of thorium, a detector with high energy resolution and high sensitivity is necessary. Unlike the conventional gamma-ray detectors used in previous lunar missions, *Kaguya* for the first time carried a cylindrical germanium crystal as the main detector, with a volume of 252 cm^3 (Hasebe et al. 2009a), instead of NaI(Tl), which has limited energy resolution and had been employed by the *Apollo* orbital spacecraft and the *Lunar Prospector* (Hasebe et al. 2009b). At an altitude of 100 km, the spatial resolution of the *Kaguya* GRS had a range of 100–140 km, which was 10–15 times higher than the *Lunar Prospector* GRS and 8–13 times better than the *Apollo* GRS (Kobayashi et al. 2010), as well as 10 times better than the *Chang'e 1* GRS (Yamashita et al. 2010) (Fig. 8). A total of 2674 h of effective observation time are applied for the measurements of lunar gamma rays (Yamashita et al. 2010).

The relative distribution of U and Th over the whole Moon (Fig. 9) indicates that the highest abundances are found in the Procellarum KREEP Terrane, especially in the Copernicus crater, Montes Jura, and the Apennine Bench. Relatively low abundances were recorded in Mare Imbrium, Mare Tranquillitatis, and the highlands on the lunar farside, and the South Pole–Aitken Terrane is higher in abundance than surrounding areas.

There is general agreement about the distribution of thorium in each region of the lunar highlands (Fig. 9), but the distinct variation in the average abundance of uranium between

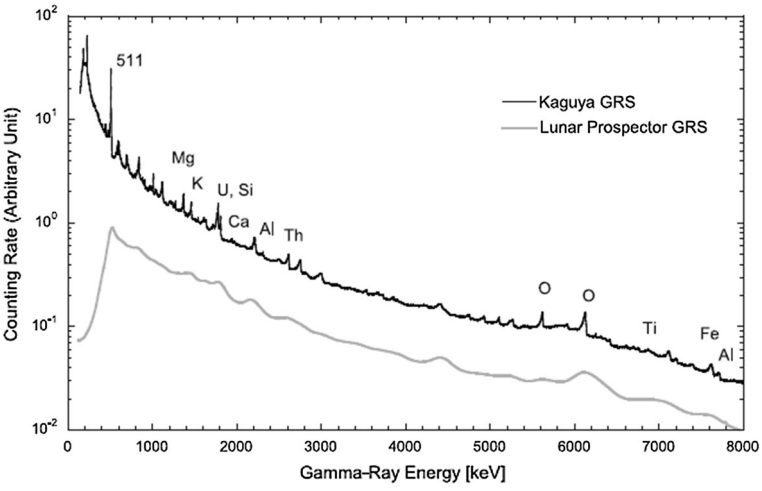

Fig. 8 Comparison of energy sensitivity between the *Lunar Prospector* and *Kaguya* gamma-ray spectrometers [used by permission of John Wiley and Sons Inc., after Yamashita et al. (2010), Fig. 1]

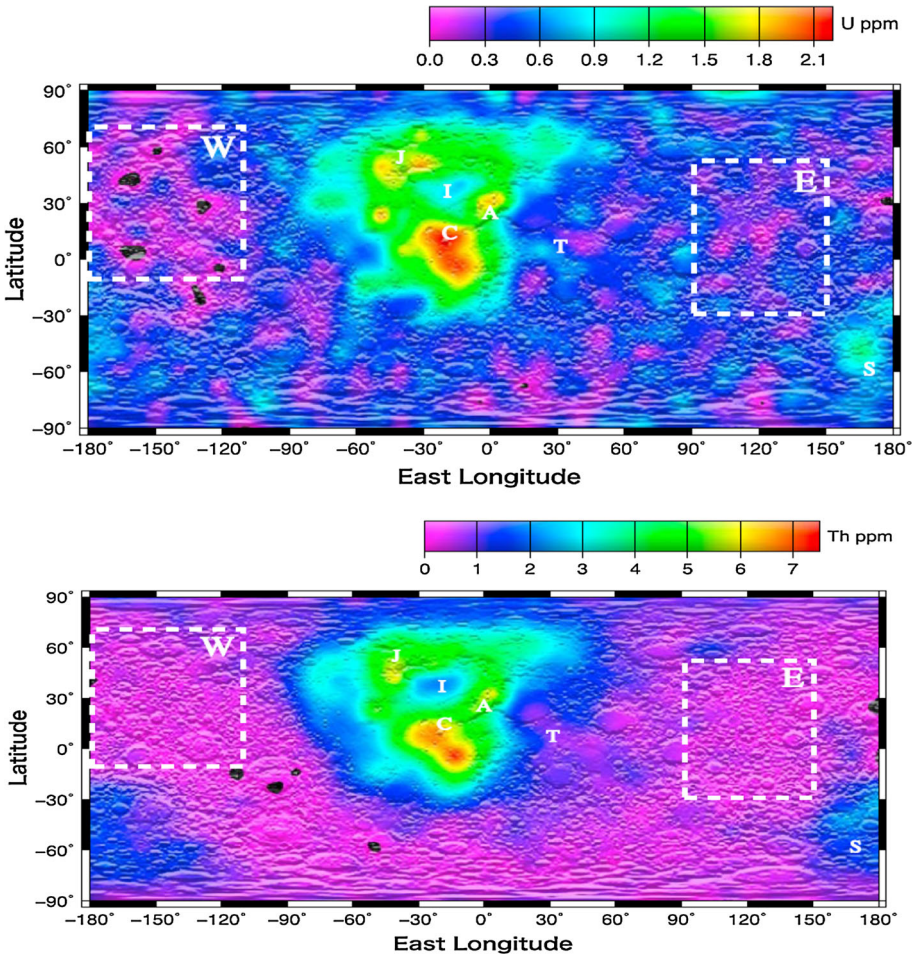

Fig. 9 Distributions of lunar surficial U (*left*) and Th (*right*) measured by the *Kaguya* GRS based on 90 latitude × 90 longitude pixel data: (*A*) Apennine Bench; (*C*) Copernicus; (*I*) Mare Imbrium; (*J*) Montes Jura; (*S*) South Pole–Aitken Terrane; (*T*) Mare Tranquillitatis. *Dotted area* labeled "*E*" and "*W*" indicate the east and west highland regions, respectively [used by permission of John Wiley and Sons Inc., after Yamashita et al. (2010), Fig. 3 and Fig. 4]. (Color figure online)

the east and west highlands was first identified by the *Kaguya* GRS. This difference in distribution between U and Th implies the individual evolution of the lunar crust in the two regions on the farside. Alternatively, uranium and thorium are so similar in volatility and incompatibility that it was unlikely for uranium to fractionate from thorium in the absence of water during igneous processes (Yamashita et al. 2010). This discovery will contribute to new views of the evolution of igneous activities and the lunar highland.

3.2 Distributions of Olivine and Mg-Spinel

Earth's mantle is mainly composed of olivine and its high pressure spinel and perovskite versions, and thus the global distribution of olivine on the Moon is essential to improve the

understanding of the evolution of the lunar mantle. When mixed with pyroxene, the spectral absorption features of olivine are extremely difficult to characterize with only near-infrared spectra, even at high spectral resolution (Singer 1981), only when olivine is present at >30 % of the mafic mineral content of rocks (Cloutis et al. 1986) the diagnostic absorption feature around 2 μm can be detected. Early studies of the lunar distribution of olivine were based on Earth-based telescopic observations. Only two olivine-rich sites were reported as a result of the low spatial resolution. Higher accuracy ultraviolet–visible data from *Clementine* in five spectral channels between 0.4 and 1.0 μm identified five additional sites with exposed olivine. Later, Yamamoto et al. (2010) pointed out that the continuous spectral reflectance data from the Spectral Profiler (SP) on *Kaguya* could bring more accurate identification of olivine-bearing sites than the separated spectral information from *Clementine*. Based on these new data, only the Theophilus crater among these five sites was reported to be rich in olivine by Yamamoto et al. and an additional 31 olivine-rich sites including Oceanus Procellarum and some craters' rims such as Maria Crisium, Moscoviense, and Imbrium, have features diagnostic of olivine (see Fig. 10). The locations of olivine-rich sites are associated with large impact basins with relatively thin crust. As the spectral band used for assessment of the distribution of olivine is constrained to between 0.7 and 1.6 μm in SP (Yamamoto et al. 2010), these results should be reexamined in order to remove the spectral contribution of pyroxene. The global data with higher resolution in 85 spectral channels from 400 to 3,000 nm highlighted those areas rich in exposed olivine (Isaacson et al. 2011). So far, the Copernicus and Aristarchus craters have been confirmed to feature absorption signatures consistent with olivine from data of all missions, including Earth-based telescopes (Pieters 1982; Lucey et al. 1986), the *Clementine* UVVIS (Tompkins and Pieters 1999; Lucey 2004), *Kaguya* SP (Yamamoto et al. 2010), and *Chandrayaan 1* M^3 (Isaacson et al. 2011; Mustard et al. 2011; Dhingra et al. 2013; Bugiolacchi et al. 2011) (Fig. 10). In addition, the Marius crater around the Marius Hills, Mare Moscoviense, and the Schrödinger basin have been

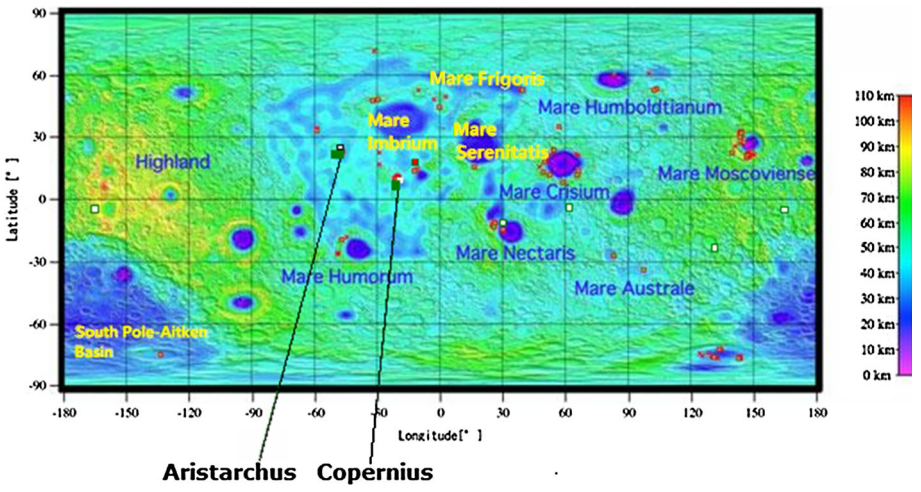

Fig. 10 Relation between the global distribution of olivine-rich sites (*red points* based on *Kaguya* SP observations by Yamamoto et al. 2010, 2012 and M^3 by Isaacson et al. 2011, Thaisen et al. 2011, Besse et al. 2011, and Kramer et al. 2013; *white points* based on *Clementine* by Tompkins and Pieters (1999) and Lucey (2004); *dark green points* based on the two missions above and M^3 by Isaacson et al. 2011, Mustard et al. 2011, and Dhingra et al. 2013, and Earth-based observations by Pieters (1982) and Lucey et al. 1986) and the lunar crustal thickness [reproduced and used by permission of Nature Publishing Group, Yamamoto et al. (2010), Fig. 10]. (Color figure online)

confirmed with data from SP (Yamamoto et al. 2010, 2012) and M^3 (Isaacson et al. 2011; Thaisen et al. 2011; Besse et al. 2011; Kramer et al. 2013). Most of the exposed olivine is located at the rims of craters, not at the central peaks.

The origin of olivine, whether it is consistent with dunite or troctolite, is significant to understanding the origin and evolution of the magma ocean. Another difficulty is to distinguish each composition of the mixture composed by plagioclase and mafic minerals like pyroxene or olivine. Given the lack of a consistent association between plagioclase and olivine, Yamamoto et al. (2010) probably erred in favoring that olivine exposures is originated by lunar mantle and more consistent with dunite rather than troctolite. A method based on olivine's Mg# (molar Mg/Mg + Fe) proposed by Isaacson et al. (2011) can explain the origin of the olivine, such as Mg-rich olivine around Mare Moscovience and Copernicus crater should be associated with mantle source and/or dunite. Alternatively, the absorption beyond 1,600 nm spectral band in M^3 data caused by inclusion of Cr-spinel (chromite) is common in lunar olivine. Isaacson and Pieters (2010) developed a modified Gaussian model deconvolution to avoid the influence of chromites and then to evaluate the accurate composition of olivine. In addition, the discovery of a new rock type, Mg-spinel bearing olivine, around the Copernicus crater (Dhingra et al. 2013) and Mare Moscoviense (Pieters et al. 2011) will also provide indirect clues to the origin and evolution of the olivine.

3.3 Distribution of Pure Anorthosite

The presence of anorthosite on the Moon was proposed based on previous results from ground-based spectroscopy. Discovery of an absorption band centered near 1250 nm by the Multiband Imager (MI) on *Kaguya* with high spatial resolution of 62 m contributed to accurate measurements of the global distribution of anorthosite on the Moon (Ohtake et al. 2009). The pure anorthosite (PAN), composed of nearly 100 % anorthite (about 98 vol. %) was exposed in many locations, such as the South Ray site, the Tycho and Tsiolkovskiy craters, and Mare Orientale (Fig. 11).

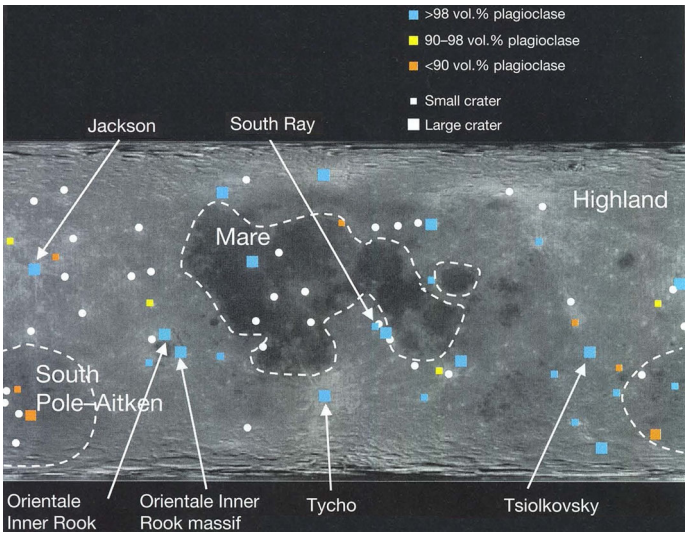

Fig. 11 Global distribution of exposed anorthosite (*blue squares*) [reproduced and used by permission of Nature Publishing Group, after Ohtake et al. (2009), Fig. 1]. (Color figure online)

PAN rocks occur in craters with diameters exceeding 30 km, which have been excavated to a depth of 3 km. The largest crater with PAN rocks exposed on the Moon is Tsiolkovskiy (a depth of 30 km was penetrated by the impact). In other words, the upper crust, ranging from 3 to 30 km, was probably composed of PAN rock. The global distribution of PAN is probably segregated and crystallized from the magma ocean, or may be produced by similar deformations as occurred on Earth (Lafrance et al. 1996).

3.4 Distribution of Silicate Rocks and Highly Evolved Magma

Silicate rocks and their formation mechanism are important to understanding the evolution of the late-stage, highly evolved lunar magma ocean. Insensitive spectrum band of UV/visible/NIR and GRS spectroscopy and lower spatial resolution or inadequate coverage in previous missions cannot identify important lunar silicate rocks, including quartz, silica-rich glass, alkalis and feldspars. The three Diviner "8 μm" thermal infrared channels (7.55–8.05, 8.10–8.40, and 8.38–8.68 μm), with a spatial resolution of 200 m, are sensitive to these silicate minerals (Greenhagen et al. 2010). Figure 12 shows laboratory spectra from these channels of silicate and typical mafic and ultramafic rocks. In this figure, the Christiansen feature (CF) (Conel 1969; Greenhagen 2009) (*black arrows*), that is, the maximum of the curve, can be used to assess the silicate content of materials on the lunar surface. The most silicate-rich materials, such as quartz and silicate-rich glass, exhibit CF positions far below 8 μm, while those with more mafic minerals lie beyond 8 μm. The CF position of anorthite is located at just 8 μm. Therefore, the averaged CF positions of lunar surface materials indicate silicate mineral content. Moreover, the silicate mineral content indicated by the combined characters of spectral slope *I* (*I*, ε3–ε4, where ε3 and ε4 are emissivities in channel 3 and 4, respectively) and the concavity of the curves *c* (the direction of concavity between channels 3–5) calculated with the three 8 μm channels are

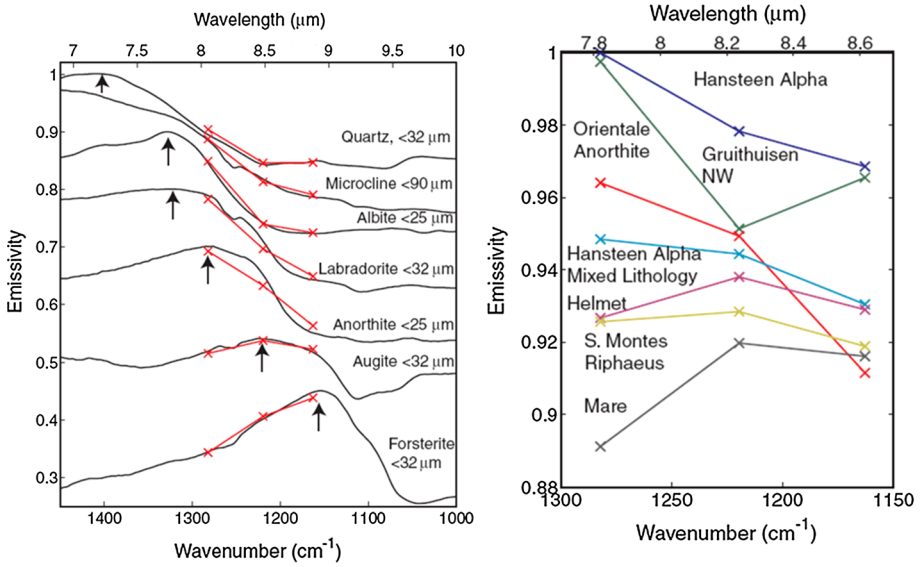

Fig. 12 Experimental spectra of major rock-forming minerals (*left*) and calculated CF values for some lunar regions from Diviner (*right*) [used by permission of American Association for the Advancement of Science, after Glotch et al. (2010), Fig. 2 and Fig. 4]

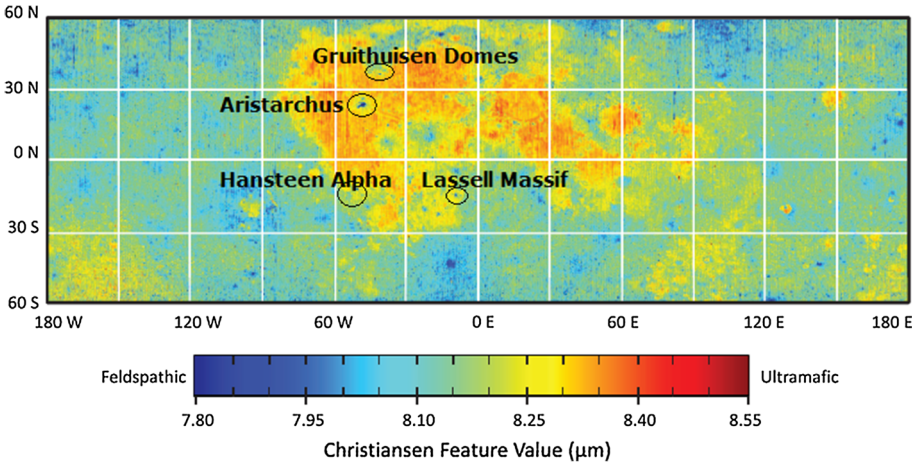

Fig. 13 CF values on the lunar surface for silicate mineralogy [reproduced and used by permission of American Association for the Advancement of Science, after Greenhagen et al. (2010), Fig. 2]. (Color figure online)

consistent with those features from CF positions (Glotch et al. 2010). The positive slope and concave-upward spectra are properties of silicate-rich materials, otherwise are those of mafic and ultramafic materials.

A CF value for global distribution and some detailed regions of silicate mineralogy is illustrated in Fig. 13. The averaged CF values at highland regions, dominated by plagioclase feldspar, are smaller than those at lunar maria, covered by basaltic materials. In particular, four lunar "red spot" featured with ultraviolet absorption exhibit highly silicate characteristic. They are the Gruithuisen Domes, the Aristarchus crater, Hansteen Alpha, and the Lassell Massif (Fig. 13). Moreover, the particular albedos and morphologies at the four red spots are interpreted as characters of volcanic cumulodomes with viscosity. The low FeO values and high Th abundances of these domes are consistent with terrestrial rhyolites or alkali-suite lithologies such as granites. Intermediate and acid rocks exposed at the Marian Domes adjacent to Gruithuisen and Compton-Belkovich on the lunar farside and the four "red spots" are indicative of highly evolved magma processes (Greenhagen et al. 2010; Glotch et al. 2010; Glotch et al. 2011; Jolliff et al. 2011). Silicate lithologies on the Moon probably occur as a result of intrusive plutons or extrusive lava. The preferred mechanism for this generation is basaltic underplating: in the late stages of the magma ocean, the basaltic magma beneath intrudes into the lunar crust transferring anorthosite into silicic magmas in the process, causing exposure of the rhyolite plumes on the surface or the generation of silicate plutons at depth (Glotch et al. 2010).

4 Improved Knowledge of Interior Structures by New Lunar Gravity Models and Reanalysis of Apollo Seismic Data

4.1 Gravity Models from Direct Detection of Global Tracking Data

Since the Moon rotation is synchronous to its revolution around the Earth, only gravity field on lunar nearside has not been accessible until recently. Indeed, the GLGM-3, the standard gravity model, with the highest spherical harmonic degree and order of 150,

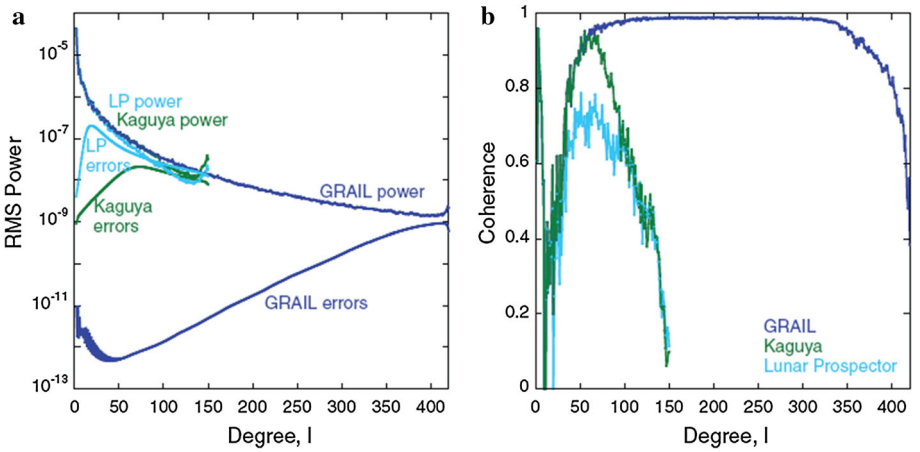

Fig. 14 **a** RMS power and **b** coherence versus harmonic degree for the gravity fields determined by *GRAIL*, *Kaguya* and the *Lunar Prospector* [used by permission of American Association for the Advancement of Science, after Zuber et al. (2013a), Fig. 2]

constructed by Mazarico et al. (2010) using all NASA historical orbits from the *Lunar Orbiters* and the *Apollo* subsatellites, *Clementine*, the *Lunar Prospector*, and even *LRO*, has an effective degree and order over the farside of only 15 (Konopliv et al. 2013). So far, there have been two approaches to solving this problem.

Through a relay satellite such as *Okina* (formerly Rstar) in the *Kaguya* mission, four-way Doppler (Namiki et al. 2009) technology was applied to directly observe the tracking data of the main orbiter over the far side (Iwata et al. 2010). The *Kaguya* main orbiter was maintained in polar circular orbit at a latitude of 100 km, and *Okina* was controlled into an elliptical orbit from 2,400 to 100 km (see Iwata et al. 2010, Fig. 1). The lunar gravity solutions derived from these global tracking data include SGM90d (Namiki et al. 2009), SGM100h (Matsumoto et al. 2010), and SGM100i (Goossens et al. 2011), of which SGM100h was constructed with historical tracking data and all usable four-way Doppler tracking data for 14.2 months and SGM100i were further improved using additional S-band differential VLBI data. The direct orbital tracking data significantly improved the resolution of the gravity field over the farside, equal to information up to about harmonic degree 70 (Matsumoto et al. 2010), and the accuracy of the low-degree harmonic coefficients was improved as well (see Fig. 14). The formal uncertainty of the gravity anomalies averaged over the far side is 49 mGal in GLGM-3 and 35 mGal in SGM100h, whereas the error over the nearside of 10.5 mGal in GLGM-3 is better than the 26 mGal in SGM100h (Mazarico et al. 2010; Matsumoto et al. 2010), because of the lower altitude of the *Lunar Prospector* during its extended mission, which was capable of extracting information from higher spherical harmonic degrees and identifying the small-scale mass variation on the nearside. Therefore, only the localized formal errors could underestimate the total gravity field errors. Even the SGM100h model still has large uncertainties for small-scale gravity anomalies in the northern hemisphere on the lunar farside because of an inadequate coverage rate there (Matsumoto et al. 2010).

Another approach to map the gravity anomalies over the far side is to observe the changes in distance between two satellites caused by gravitational variation using satellite-to-satellite (SST) technology. This tracking method, similar in principle to the *Gravity Recovery and Climate Experiment(GRACE)* for Earth gravity exploration, was applied in

the *GRAIL* mission to detect lunar gravity. The twin spacecraft, with intersatellite spacing of around 80–220 km, were maintained in lunar orbit at an altitude of around 50 km in primary mission for 90 days (from 1 March to 30 May 2012; Zuber et al. 2013a) and then were lowered to 23 km in extended mission for about 100 days (from 29 August to 12 December 2012; Zuber et al. 2013b). Afterward, two new lunar gravity models, GL0420A (13 km) and GL0660B (8.3 km), were constructed, the latter with combined DSN and Ka-band range rate data for 3 months during the *GRAIL* primary mission. The results also benefit from the large quantity of measurements supported by the Ka band with interval sampling of 5 s and 4 orders-of-magnitude higher accuracy than the S-band 10 s data sample times in previous missions (Konopliv et al. 2013).

To understand the advantages and disadvantages of these gravity solutions, the methodologies employed to solve these models must be taken into consideration. It should be noted that although the orbital data have been supplemented by recent missions, there are still gaps over the far side and inadequate coverage over the whole Moon, which can cause large uncertainties on RMS power at high degree and order. A common approach to deriving the coefficients at high degree and order is a power spectrum constraint, such as Kaula's rule (Kaula 1966). Prior to *Kaguya*, to obtain robust estimation of high-degree coefficients, the preferred $\beta = 2.5$ in Kaula's rule was applied to build the LP165P (Konopliv et al. 2001) and GLGM-3 (Mazarico et al. 2010) models. After that, to reduce the influence of the small gaps in the northern farside four-way Doppler tracking data, $\beta = 3.5$ was chosen for calculating the coefficients beyond degree 70 (Matsumoto et al. 2010; Goossens et al. 2011). Even in the most accurate model, GL0660B, to extend the higher coefficients to degree 420, estimated to be the maximum global resolution of the *GRAIL* data, the similar constraint of $\beta = 3.6$ was optimal (Konopliv et al. 2013). Although a better choice of the spectrum constraint is helpful to build more robust coefficients at high degree, the actual degree strongly depends on the quality and coverage of the tracking data. Compared with the models developed by the *Lunar Prospector* and *Kaguya*, those from *GRAIL* demonstrate that there are very high coherences between gravity and topography up to higher degree (Fig. 15). It is also indicative of capability to extract features in small-scale of about 17 km (320 degree and order) gravity anomalies, including the mascon basins' compensation states, thermal evolution of the Moon, and even local magmatism (Zuber et al. 2013b). Zuber et al. (2013a) have claimed that, from degrees 80 through 300, over 98 % of the gravitational information is contributed by topography and only the remaining 2 % represents the interior structures of the Moon.

4.2 Research on Origin of Mascons

In Bouguer anomaly maps from GL0660B (Fig. 15b), the highlands on the lunar far side possess negative anomaly, but Oceanus Procellarum and the South Pole–Aitken Terrane are characterized by positive anomalies, and many mare basins have high-amplitude positive anomalies, referred to as mascons ("mass concentrations"; Muller and Sjogren 1968). The free-air anomaly of most mascons is bull's-eye shaped, with a positive free-air anomaly center within concentric negative rings, surrounded by an outer positive ring. These include Mare Orientale, Mare Moscoviense, the Freundlich-Sharonov basin, and the Humorum basin (Fig. 15). The remaining mascons possess only a positive-gravity anomaly center, including large mare basins on the near side such as Mare Imbrium and Mare Serenitatis (Fig. 15). The origin of the mascons has been accounted for without a definitive explanation for several decades. Because of the small effect of the mare fills exposed on the surface of mascon basins, the central positive-gravity anomaly has been attributed to

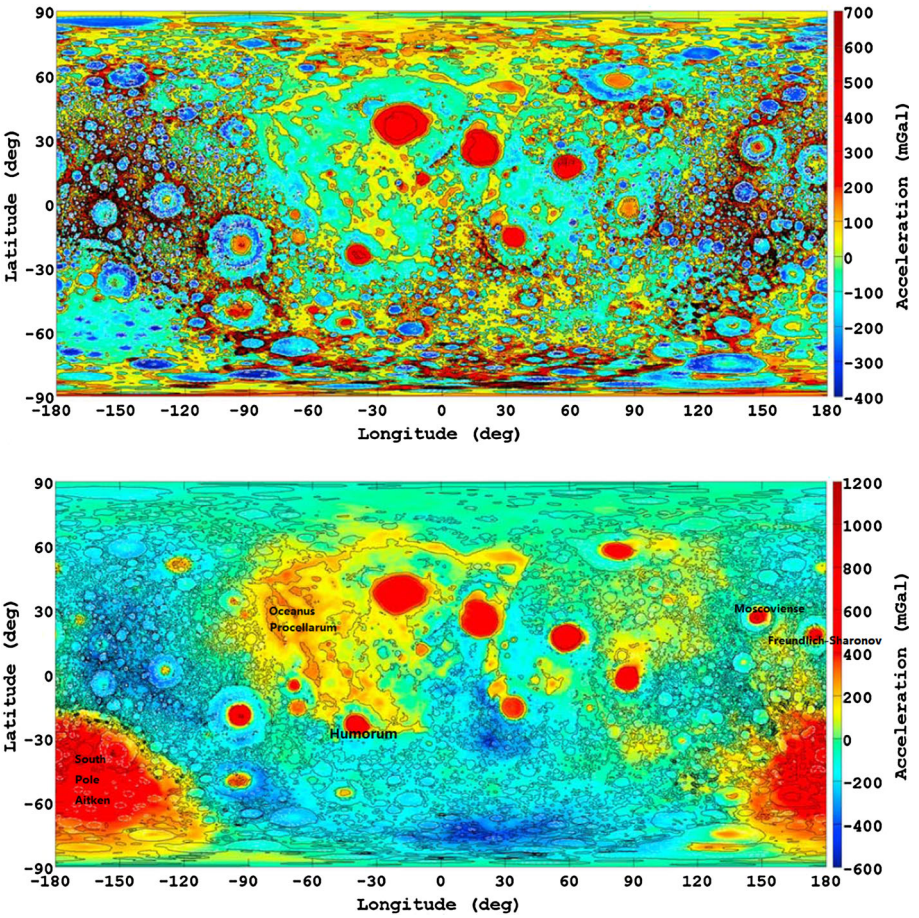

Fig. 15 Maps of *GRAIL* (*left*) free-air and (*right*) Bouguer lunar gravity anomalies from *GRAIL* gravity model GL0660B [used by permission of John Wiley and Sons Inc., after Konopliv et al. (2013), Fig. 10]. (Color figure online)

uplifted mantle beneath the basins (Neumann et al. 1996) or, more recently, flexural uplift of a thickened annulus caused by subisostatic crust (Andrews-Hanna and Stewart 2011; Andrews-Hanna 2012). To confirm the latter explanation, Melosh et al. (2013) used a hydrocode to simulate the impact process to form the original bull's-eye anomaly with a negative center and a finite-element model to simulate flexural uplift of an annulus caused by subisostatic post impact processes to drive the central anomaly positive. It would be worthwhile to further consider the detailed assumptions upon which this simulation were based, including the composition and temperature conditions of the lunar crust and the mantle and crustal thickness.

4.3 Reanalysis of Apollo Seismic Data

The ALSEP (Apollo Lunar Surface Experiments Package) included active and passive seismic experiments, of which the former provide the ways to research structures near the surface because of limited spatial offset between the site of the source and the geophones

(3–6,000 m) (Kovach et al. 1973), and the latter are employed to investigate the deep structures of the Moon, including the crust, the mantle and the core. In the passive seismic experiments, Apollo seismic network was composed of four stations in a equilateral triangle at the Apollo 12, 14, 15 and 16 landing sites with 1,000 km spacing for each side, of which the station A12 and A14 were deployed with spacing of 180 km. Apart from apparent limitations including restriction in durations in acquisition and bandwidth, aerial extent of the network and the number of stations, it is the most important that the reliability of detection of lunar interiors was strongly relied on the origin of the moonquakes and characteristics of their seismic signals. More than 13,000 seismic events in total until 2008 (Nakamura et al. 2008) have been identified in Apollo experiments, of which over 12,500 were detected by the long-period seismometers (Nakamura 2010). In addition, new events have been being identified recently. The moonquakes include shallow but large magnitude events, deep but small events, and small seismic disturbances by thermal variation on lunar surface, as well as others caused by external factors including several man-made and numerous meteoroid impacts. Almost every moonquake was restricted on the nearside, and only a few possible deep moonquakes on the farside have been identified (Nakamura 2005). These play a crucial role in understanding structures of the mantle and even the core, although there has not been a definitive conclusion. Detailed information of moonquake sources and their distributions are shown in Table 2 and Figure 10 in Gagnepain-Beyneix et al. (2006). The distributions of seismic events in Figure 10 in Gagnepain-Beyneix et al. (2006) and their seismological features suggest that the limited regions in lunar crust and mantle on the nearside was the only to be able to detected. Further, the velocity variation of the interiors in these regions was ambiguous because of the limited range of seismic returns detected by just four seismometers. Additionally, the characteristics of signals detected which have high frequency and anomalous long duration caused by intense scattering and weak attenuation of regolith make it additionally difficult in data processing. Meanwhile, the characteristics of high attenuation of partial melt region around core-mantle boundary prevent the seismic signals originated from farside from penetrating through it (Table 2).

In the twenty first century, new analytical tools were employed to reanalyze the seismic data, including nonlinear inversion (Khan et al. 2000; Khan and Mosegarrd 2002), array stacking technology (Weber et al. 2011) etc. The advantages of nonlinear inversion based on Monte Carlo algorithm to previous linear hypothesis was to delineate more realistic interior structures and then determined the thickness of the crust (30–40 km), which was consistent to that estimated based on GRAIL data (Wieczorek et al. 2013). Given the complex features of seismic signals and moonquakes, array stacking technology was applied to improve the signal-to-noise ratio of seismic wave and then to estimated structures within lunar core (Weber et al. 2011).

Additional information of the lunar interiors has been derived by integrating newly acquired data sets including gravity models from GRAIL and chemical composition from multispectral remote sensing. New sights of the lunar interior will be derived from integration of a diverse range of geophysical approaches. In recent investigations, composition and temperature parameters of the Moon were estimated by Khan et al. (2007) and Kronrod and Kuskov (2011) based on joint inversion of Apollo passive seismic data and the mass and the moment of inertia from Lunar Prospector under the hypothesis of thermodynamic properties of minerals, which presents the relationship of seismic velocities and density of the minerals with their compositions under a certain temperature and pressure. However, this inversion process was not able to avoid the inherent non-uniqueness of solutions in geophysics and uncertainty in mineralogical physics, and to exclude influences by tectonics

and variation of rock phase. On the other hand, joint inversion of Apollo seismic data and GRAIL induced gravity model was applied to directly construct variations of density and velocity with depth (Weber and Schemerr 2014). The complementary property of these data reduced the inherent non-uniqueness in seismological and gravity inversion. Meanwhile, the more realistic crustal thickness estimated with GRAIL data further reduced uncertainty estimates of velocity in mantle and core.

Research on density and velocity models for shallow structures including the lunar crust will be the focus of future work. It will facilitate understanding of the structures within the mantle and possible core too. Integration in methodology including studies of remote sensing and topography will aid the understanding of shallow structures.

4.4 Interior Structures and Materials

Estimating the thickness of lunar crust is the most key to the understanding of the interior structure and evolution of the Moon. The average global thickness can also be independently estimated by Wieczorek and Phillips (1998) with a gravity model from the Clementine mission. Ishihara et al. (2009) used the SGM100 g gravity and STM359_grid-03 topographic models to calculate the Moho relief with no prior seismic constraints at the *Apollo 12* and *14* landing sites. The estimated average crustal thickness is close to 50 km, with 45.1 and 49.9 km at *Apollo 12* and *14* sites, respectively, consistent with 45 ± 5 km derived by Khan et al. (2000) with seismic data. Nevertheless, a relatively high lunar crust density of 2,800 kg/m^3 was used for the gravity inversion. A more reliable average density was evaluated by Wieczorek et al. (2013) using *GRAIL* data to be 2,550 ± 18 kg/m^3. The average porosity in the crust afterward was also estimated to be 12 %. With two special constraints from the seismically determined average thickness of 30 or 38 km near the

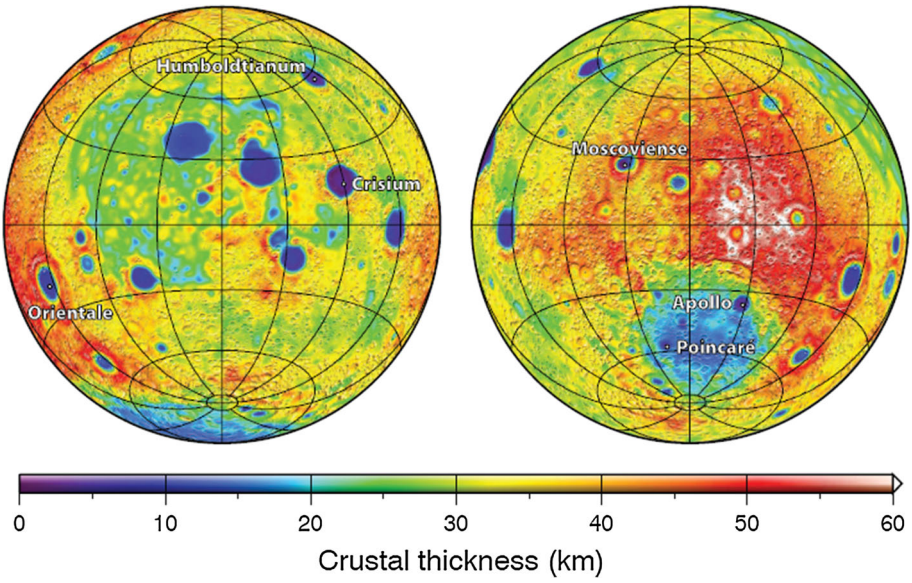

Fig. 16 Estimates of lunar crustal thickness over the nearside (*left*) and farside (*right*) from *GRAIL* gravity and LOLA topographic models [used by permission of American Association for the Advancement of Science, after Wieczorek et al. (2013), Fig. 3]. (Color figure online)

Apollo 12 and *14* landing sites and a minimum crustal thickness around the whole Moon, the average crustal thickness was estimated at 34–43 km (Fig. 16), and the thickness in the Moscoviense and Crisium basins is nearly zero, which is consistent with the exposures of olivine from the lunar mantle (Fig. 10; Yamanoto et al. 2010; Isaacson et al. 2011; Thaisen et al. 2011). These results include a high uncertainty in the areas covered solely by mare basalts. Future work will include estimates of the vertical and lateral variations in density.

More tectonic features and structures have been identified, including volcanic landforms and crater-forming and large linear structures. Many linear anomalies relating to the tectonics and magmatism of the Moon were identified in the Bouguer gradient map in Fig. 1 of Andrews-Hanna et al. (2013).

5 Subsurface Structure Detected by Lunar Radar Sounding

The subsurface of the Moon was first investigated by the Lunar Sounder Experiment (ALSE) on board the *Apollo 17* spacecraft, with three frequency ranges centered on 5 MHz (HF1), 15 MHz (HF2) and 150 MHz (VHF) (Phillips et al. 1973a, b). For comparison, the HF1 frequency was also used as the main frequency for the *Kaguya* Lunar Radar Sounder (LRS; Ono et al. 2010). Compared with ALSE, the LRS is capable of identifying the shallow subsurface interface due to its higher vertical resolution, but this is not the only reason different subsurface layers have been found by ALSE and LRS in the same region (Peeples et al. 1978; Cooper et al. 1994; Ono et al. 2010). The major difficulty in reliably detecting subsurface echoes is surface clutter suppression. Intense and numerous signals from surface off-nadir echoes are always superposed on the weak subsurface nadir echoes, especially when the subsurface to be detected is very shallow, while intense signals are also likely to produce an illusory subsurface that can be confused with the real subsurface interface. This is commonly referred to as clutter or backscatter noise (Phillips et al. 1973b; Peeples et al. 1978). As the surface backscatter signals from the same site could be suppressed by correlation summation of adjacent-orbit data, the multiple orbit correlation (MOC) technique was proposed and used to reduce the clutter noise for ALSE (Peeples et al. 1978; Cooper et al. 1994) and LRS (Ono et al. 2009; Oshigami et al. 2009). However, the application of the MOC method is restricted to regions with a relatively smooth and continuous subsurface. Another approach is based on topographic data to simulate the surface echo, which is then subtracted from the radar sounding measurements; this has been used not only for LRS (Kobayashi et al. 2002a, b) but also for SHARAD onboard the *Mars Reconnaissance Orbiter* (Croci et al. 2011).

The regions observed by ALSE and LRS and their ground tracks are shown in Fig. 17 (Cooper et al. 1994; Ono et al. 2009). Although similar frequencies were employed by both missions, the actual depths of subsurface echoes were different. In Mare Serenitatis, two reflectors at depths of 0.9 and 1.6 km were detected by ALSE (Peeples et al. 1978; Sharpton and Head 1982), but a unique reflector at 175 m was detected by LRS (Ono et al. 2009). The reflections detected by ALSE and LRS for other areas are listed in Table 3. Furthermore, wavy reflectors in sounding profiles in Mare Serenitatis observed by ALSE and LRS are most likely to be consistent with anticline stratigraphic interfaces under the mare ridges (Peeples et al. 1978; Ono et al. 2009). In Fig. 18, the red lines in the shapes of anticlines are parallel to the topographic relief of the mare ridge.

According to the distributions of exposed basaltic units in Mare Serenitatis deduced from morphology, albedo, and other spectral properties, the subsurface reflecting horizons have been interpreted as interfaces between mare basalts that erupted in different volcanic events (Sharpton and Head 1982; Ono et al. 2009). Figure 19 illustrates that the boundaries between S11 and other stratigraphic horizons in profiles c–c′, d–d′, and e–e′ are consistent

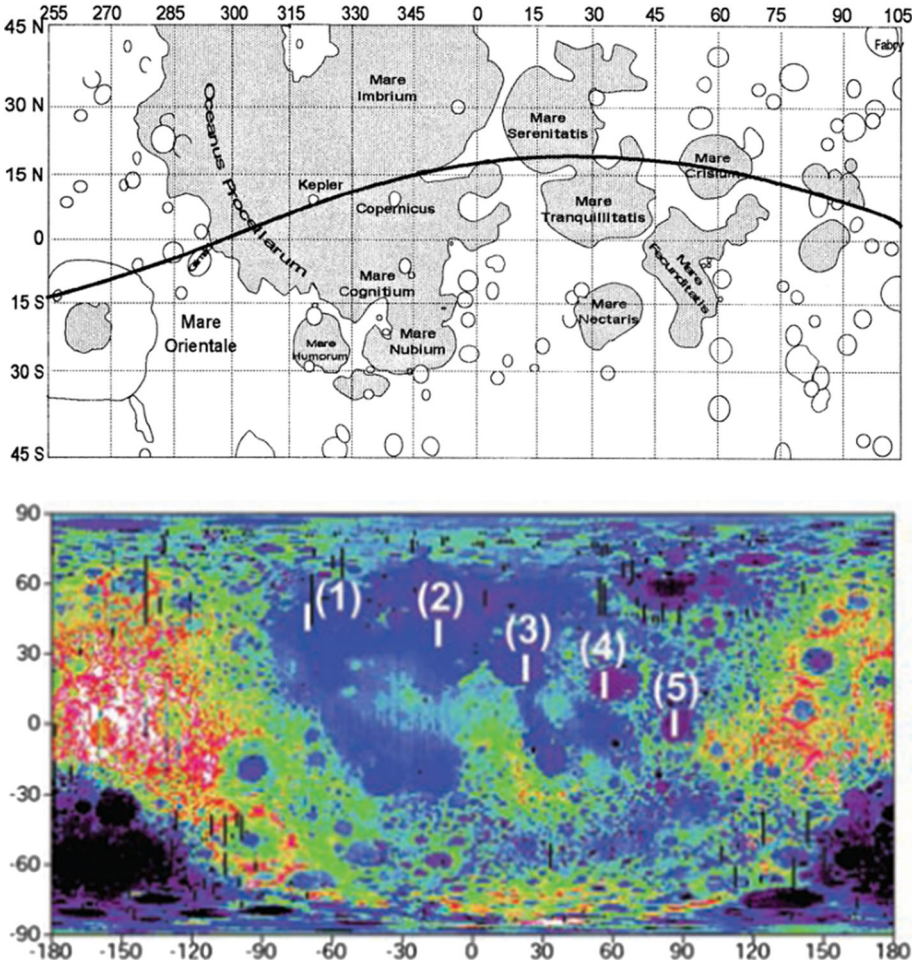

Fig. 17 Ground tracks of measurements by ALSE (*left*) [used by permission of John Wiley and Sons Inc., after Cooper et al. (1994), Fig. 9) and LRS (*right*) [used by permission of American Association for the Advancement of Science, after Ono et al. (2009), Fig. 1]

Table 3 Reflector echoes detected by ALSE and LRS

	Procellarum (m)	Imbrium (m)	Crisium	Serenitatis	Smythii (m)
ALSE[a]	1,690		1.4 km	0.9, 1.6 km	
LRS[b]	160, 347	250, 460	145, 660 m	175 m	250

[a] Peeples et al. (1978); Cooper et al. (1994); Sharpton and Head (1982)

[b] Ono et al. (2009)

with the distributions of basaltic units on lunar surface. The boundary between S15 and S28 can also be identified in profile a–a′. Further investigations demonstrate that the interfaces between basalt units erupted in distinct magmatic episodes are preferred to be buried regolith layers evolved from the debris plume by impact events. The thickness of

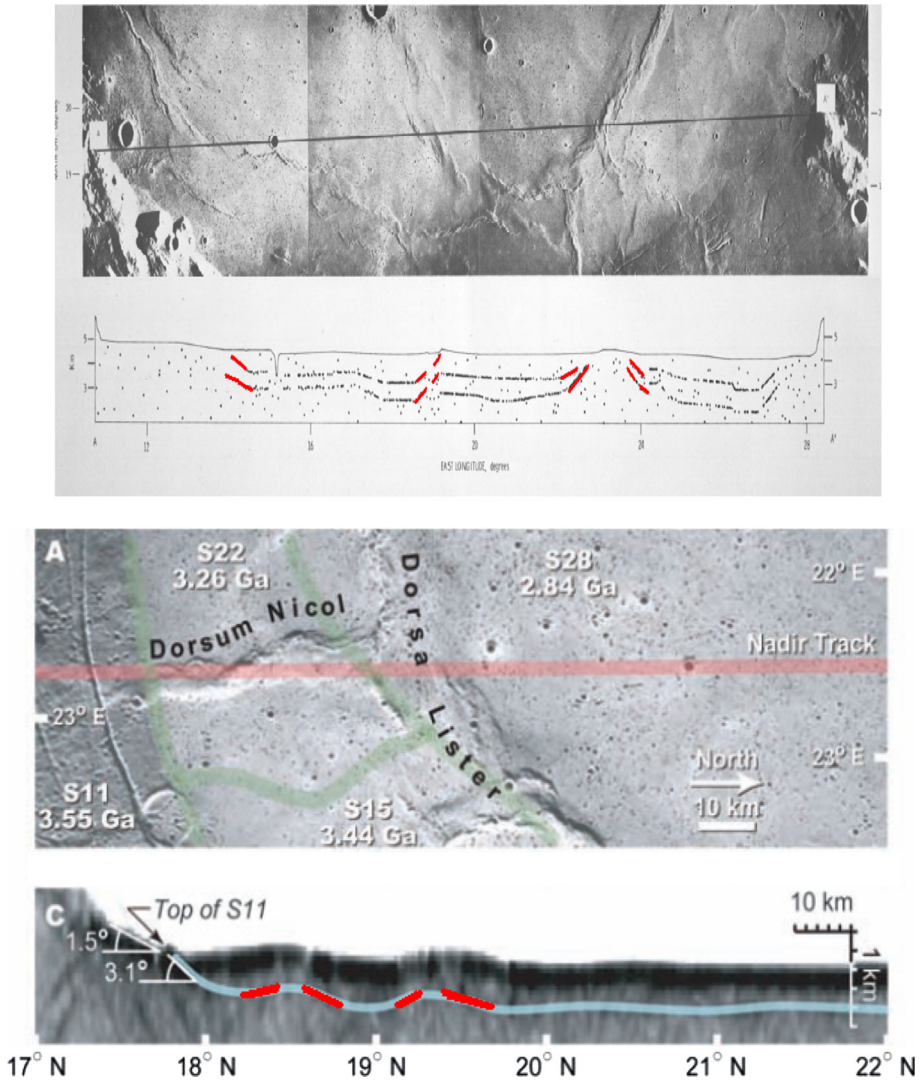

Fig. 18 Anticline stratigraphic interfaces (*red lines*) under the mare ridges along the profiles observed by *Apollo 17* (*left*) and the *Kaguya* LRS (*right*) in Mare Serenitatis [reproduced and used by permission of John Wiley and Sons Inc., after Peeples et al. (1978), *Plate 1*; reproduced and used by permission of American Association for the Advancement of Science, after Ono et al. (2009), Fig. 3]. (Color figure online)

the regolith layers is unknown but at least 2 km thick enough, to be detectable by the HF frequency of LRS.

6 New Model of Interior Structures

The combined results from radar sounding and gravity model provide knowledge of lunar interior structures. Many layered structures related to basalts erupted in different episodes

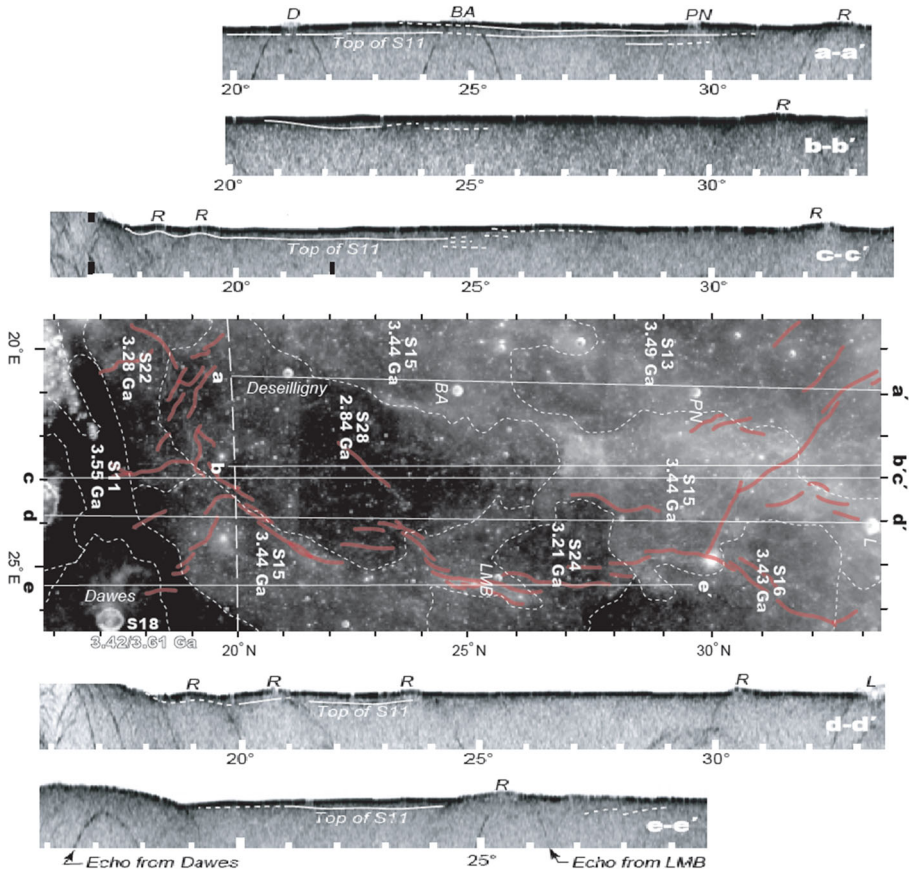

Fig. 19 Profiles in Mare Serenitatis measured by LRS [reproduced and used by permission of American Association for the Advancement of Science, after Ono et al. (2009), Fig.S3]

have formed in the lunar subsurface, such as the Procellarum KREEP Terrane (PKT) region. Furthermore, the higher concentrations of U/Th, silicate minerals, and erupted rhyolites in PKT regions indicate that residues of highly evolved magma could be preserved below the surface. Magma channels would link the underlying mafic rock basement in this region (Fig. 20).

7 Discussion

Recent missions have significantly added to our knowledge of the Moon and pointed to the direction of future planning. Comprehensive analyses of a variety of approaches, including illumination conditions, distributions of hydrogen- and hydroxyl-bearing materials, changes in CPR and temperature, and the detection of water in the Cabeus ejecta plume, have all contributed to the confirmation of the presence of water ice at the lunar poles. In future work, the distribution of hydroxyl at higher resolution and its relationship with the hydrogen abundance will be significant in determining other likely regions where water ice

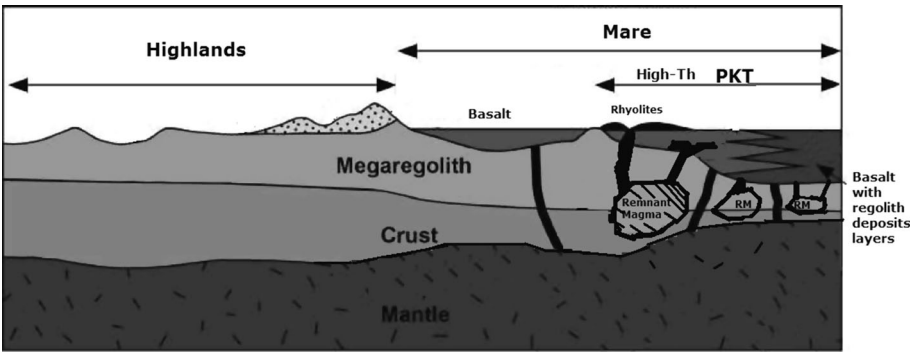

Fig. 20 Schematic diagram of new model distributions of magma residues and layered interfaces in lunar crust

could be present. Also, the variance in lunar obliquity should be taken into consideration to understand the distribution of water ice over the history of the Moon and to aid uncovering its origin and evolution.

Because of the broad band spectrum of the M^3 instrument on *Chandrayaan 1*, detailed distribution of olivine was detected at the rims of most large impact craters, and this revealed their possible relation with troctolite or mantle materials. In addition, spectral signature associated with the presence of Mg-spinel was detected by M^3. Future, highly evolved minerals, including pure plagioclase feldspar, silicate rocks, and possible rhyolites or alkali-suite lithologies, detected by the *Kaguya* MI and Diviner, will be helpful to investigate the evolution of the lunar crust and magma ocean.

The SST tracking method was first applied by the *GRAIL* mission to improve the gravity field model of the Moon, allowing the construction of the GL0660B model with degree and order 660. This gravity model has provided the highest coherence with topography so far, and it is key to the evaluation and study of small-scale anomalies, including mascons, thermal evolution, and local magmatism. Advanced lunar gravity models have yielded new understanding of the origin of the mascons and the evaluation of the lunar crustal thickness. LRS on board *Kaguya* identified and confirmed that the basaltic strata were formed in distinct episodes. To obtain reliable depths for the layered structures, the removal of surface clutter should be emphasized in future work.

Integration in methodology and new complementary data sets will be benefit to exploration of shallow structures, which will be focus for future work.

Acknowledgments We appreciate the support of Carle M. Pieters, Mark Wieczorek and Bradley L. Jolliff for the manuscript, and the permission to make use of some illustrations from Paul D. Spudis, Takahiro Iwata, and DIVINER team. We are specially grateful to Ian A. Crawford for his warm support and constructive suggestions. We sincerely acknowledge numerous valuable comments from Dr. Bugiolacchi, and rights permissions from RightsLink of reproduction of all pictures in this manuscript.

References

J.C. Andrews-Hanna, S.T. Stewart, The crustal structure of Orientale and implications for basin formation. 42nd Lunar Planet. Science Conference (2011), Abstract #2194

J.C. Andrews-Hanna. The origin of non-mare mascon gravity anomalies on the Moon. 43rd Lunar Planet. Science Conference (2012), Abstract #2804

J.C. Andrews-Hanna, S.W. Asmar, J.W. Head III, W.S. Kiefer, A.S. Konopliv, F.G. Lemoine, I. Matsuyama, E. Mazarico, P.J. McGovern, H.J. Melosh, G.A. Neumann, F. Nimmo, R.J. Phillips, D.E. Smith, S.C. Solomon, G.J. Taylor, M.A. Wiezoreck, J.G. Williams, M.T. Zuber, Ancient igneous intrusions and early expansion of the Moon revealed by GRAIL gravity gradiometry. Science **339**(6120), 675–678 (2013). doi:10.1126/science.1231753

H. Araki, S. Tazawa, H. Noda, Y. Ishihara, S. Sasaki, S. Goossens, N. Kawano, I. Kamiya. H. Otake, J. Oberst, C.K. Shum, A new lunar topographic map of the Moon by the laser altimter (LALT) on board KAGUYA, 2009-o-3-06v, http://archive.ists.or.jp/upload_pdf/2009-o-3-06v.pdf (2009a)

H. Araki, S. Tazawa, H. Noda, Y. Ishihara, S. Goossens, S. Sasaki, N. Kawano, I. Kamiya, H. Otake, J. Oberst, C. Shum, Lunar global shape and polar topography derived from Kaguya-LALT laser altimetry. Science **323**(5916), 897–900 (2009b). doi:10.1126/science.1164164

S. Besse, J.M. Sunshine, M.I. Staid, N.E. Petro, J.W. Boardman, R.O. Green, J.W. Head, P.J. Isaacson, J.F. Mustard, C.M. Pieters, Compositional variability of the Marius Hills volcanic complex from the Moon Mineralogy Mapping (M^3). J. Geophys. Res. **116**, E00G13 (2011). doi:10.1029/2010JE003725

S. Bryant, Lunar pole illumination and communications statistics computed from GSSR elevation data. American Institute of Aeronautics and Astronautics (2010), AIAA 2010–1913. doi:10.2514/6.2010-1913

R. Bugiolacchi, U. Mall, M. Bhatt, S. McKenna-Lawlor, M. Banaszkiewicz, K. Brønstad, A. Nathues, F. Søraas, K. Ullaland, R.B. Pedersen, An in-depth look at the lunar crater Copernicus: exposed mineralogy by high-resolution near-infrared spectroscopy. Icarus **213**(1), 43–63 (2011). doi:10.1016/j.icarus.2011.02.023

D.J. Burke, C.A. Dukes, J.-H. Kim, J. Shi, M. Famá, R.A. Baragiola, Solar wind contribution to surficial lunar water: laboratory investigations. Icarus **211**, 1082–1088 (2011). doi:10.1016/j.icarus.2010.11.007

D.B.J. Bussey, P.D. Spudis, M.S. Robinson, Illumination conditions at the lunar south pole. Geophys. Res. Lett. **26**(9), 1187–1190 (1999). doi:10.1029/1999GL900213

D.B.J. Bussey, M.S. Robinson, K. Edwards, A.C. Cook, T. Watters, Simulation of illumination conditions at the lunar south pole. Lunar and Planetary Science XXXII (2001), Abstract #1907

D.B.J. Bussey, K.E. Fristad, P.M. Schenk, M.S. Robinson, P.D. Spudis, Constant illumination at the lunar north pole. Nature **434**, 842 (2005). doi:10.1038/434842a

D.B.J. Bussey, J.A. McGovern, P.D. Spudis, C.D. Neish, H. Noda, Y. Ishihara, S.A. Sorensen, Illumination condition of the South pole of the Moon derived using Kaguya topography. Icarus **208**, 558–564 (2010). doi:10.1016/j.icarus.2010.03.028

D.B. Campbell, B.A. Campbell, L.M. Carter, J.L. Margot, N.J. Stacy, No evidence for thick deposits of ice at the lunar south pole. Nature **443**, 835–837 (2006). doi:10.1038/nature05167

R.N. Clark, Detection of adsorbed water and hydroxyl on the Moon. Science **326**(5952), 562–564 (2009). doi:10.1126/science.1178105

E.A. Cloutis, M.J. Gaffey, T.L. Jackowski, R.L. Reed, Calibrations of phase abundance, composition, and particle size distributions for olivine-orthopyroxene mixtures from reflectance spectra. J. Geophys. Res. **91**(B11), 11641–11653 (1986). doi:10.1029/JB091iB11p11641

A. Colaprete, P. Schltz, J. Heldmann, D. Wooden, M. Shirley, K. Ennico, B. Hermalyn, W. Marshall, A. Ricco, R.C. Elphic, D. Goldstein, D. Summy, G.D. Bart, E. Asphaug, D. Korycansky, E. Landis, L. Sollitt, Detection of water in the LCROSS ejecta plume. Science **330**(6003), 463–468 (2010). doi:10.1126/science.1186986

J.E. Conel, Infrared emissivities of silicates: experimental results and a cloudy atmosphere model of spectral emission from condensed particulate mediums. J. Geophys. Res. **74**(6), 1614–1634 (1969). doi:10.1029/JB074i006p01614

B.L. Cooper, J.L. Carter, C.A. Sapp, New evidence for graben origin of Oceanus Procellarum from lunar sounder optical imagery. J. Geophys. Res. **99**(E2), 3799–3812 (1994). doi:10.1029/93JE03096

I.A. Crawford, K.H. Joy, M. Anand, in *Lunar Exploration, Chapter 25 Encyclopedia of the Solar System*, ed. by T. Spohn, T. Johnson, D. Breuer, 3rd edn. (Elsevier, Amsterdam, 2014), pp. 555–579 ISBN: 978-0-12-415845-0

R. Croci, R. Seu, E. Flamini, E. Russo, The SHAllow RADar (SHARAD) onboard the NASA MRO mission. Proc. IEEE **99**, 794 (2011). doi:10.1109/JPROC.2010.2104130

D. Dhingra, C.M. Pieters, J.W. Head, P.J. Isaacson, Large mineralogically distinct impact melt feature at Copernicus crater—evidence for retention of compositional heterogeneity. Geophys. Res. Lett. **40**(6), 1043–1048 (2013). doi:10.1002/grl.50255

Dino, *LCROSS Impact Data Indicates Water on Moon*. NASA Ames Research Center (2011). http://www.nasa.gov/mission_pages/LCROSS/main/prelim_water_results.html. Accessed 13 Dec 2011

F. Duennebier, G.H. Sutton, Thermal moonquakes. J. Geophys. Res. **79**(29), 4351–4363 (1974). doi:10.1029/JB079i029p04351

W.C. Feldman, S. Maurice, A.B. Binder, B.L. Barraclough, R.C. Elphic, D.J. Lawrence, Fluxes of Fast and epithermal neutrons from Lunar Prospector: evidence for water ice at the lunar poles. Science **281**(5383), 1496–1500 (1998). doi:10.1126/science.281.5383.1496

J. Gagnepain-Beyneix, P. Lognonne, H. Chenet, D. Lombardi, T. Spohn, A seismic model of the lunar mantle and constraints on temperature and mineralogy. Phys. Earth Planet. Inter. **159**(3), 140–166 (2006). doi:10.1016/j.pepi.2006.05.009

T.D. Glotch, P.G. Lucey, J.L. Bandfield, B.T. Greenhagen, I.R. Thomas, R.C. Elphic, N. Bowles, M.B. Wyatt, C.C. Allen, K.D. Hanna, D.A. Paige, Highly silicic compositions on the Moon. Science **329**(5998), 1510–1513 (2010). doi:10.1126/science.1192148

T.D. Glotch, J.J. Hagerty, P.G. Lucey, B.R. Hawke, T.A. Giguere, J.A. Arnold, J.-P. Williams, B.L. Jolliff, D.A. Paige, The Mairan domes: silicic volcanic constructs on the Moon. Geophys. Res. Lett. **38**(21), L21204 (2011). doi:10.1029/2011GL049548

S. Goossens, K. Matsumoto, Q. Liu, F. Kikuchi, K. Sato, H. Hanada, Y. Ishihara, H. Noda, N. Kawano, N. Namiki, T. Iwata, F.G. Lemoine, D.D. Rowlands, Y. Harada, M. Chen, Lunar gravity field determination using SELENE same-beam differential VLBI tracking data. J. Geod. **85**(4), 205–228 (2011). doi:10.1007/s00190-010-0430-2

B.T. Greenhagen, Ph.D, Dissertation, UCLA, 2009

B.T. Greenhagen, P.G. Lucey, M.B. Wyatt, T.D. Glotch, C.C. Allen, J.A. Arnold, J.L. Bandfield, N.E. Bowles, K.L. Donaldson, P.O. Hayne, E. Song, I.R. Thomos, D.A. Paige, Global silicate mineralogy of the Moon from the Diviner Lunar Radiometer. Science **329**(5998), 1507–1509 (2010). doi:10.1126/science.1192196

B. Hapke, Coherenct backscatter and the radar characteristics of outer planet satellites. Icarus **88**, 407–417 (1990). doi:10.1016/0019-1035(90)90091-M

N. Hasebe, E. Shibamura, T. Miyachi, T. Takashima, M. Kobayashi, O. Okudaira, N. Yamashita, S. Kpbayashi, Y. Karouji, M. Hareyama, S. Kodaira, K. Hayatasu, K. Iwabuchi, S. Nemoto, K. Sakurai, S. Komatsu, M. Miyajima, M. Ebihara, T. Hihara, T. Arai, T. Sugihara, H. Takeda, C. d'Uston, O. Gasnault, E. Diez, O. Forni, S. Maurice, R.C. Reedy, *High Performance Germanium Gamma-Ray Spectrometer On Lunar Polar Orbiter SELENE (KAGUYA)*, Transactions of the Japan Society for Aeronautical and Space Sciences, Space Technology Japan, Vol. 7 (2009a)

N. Hasebe, N. Yamashita, Y. Karoji, S. Kobayashi, M. Hareyama, K. Hayatsu, S. Nemoto, K. Iwabuchi, Y. Takeda, H. Nagaoka, K. Tsukada, O. Okudaira, S. Sakurai, S. Komatsu, E. Shibamura, M.N. Kobayashi, M. Ebihara, T. Hihara, T. Arai, T. Sugihara, H. Takeda, C. d'Uston, O. Gasnault, B. Diez, O. Forni, S. Maurice, R.C. Reedy, K. Kim, Overview of elemental distributions on the Moon observed by SELENE GRS (2009b). http://archive.iists.or.jp/upload_pdf/2009-o-3-10v.pdf

G. Heiken, D. Vaniman, B.M. French, *Lunar Sourcebook: A User's Guide to the Moon* (Cambride Univ. Press, Cambridge, 1991)

H. Hiesinger, R. Jaumann, in *The Moon, Chapter 23, Encyclopedia of the Solar System*, ed. by T. Spohn, T. Johnson, D. Breuer, 3rd edn. (Elsevier, Amsterdam, 2014), pp. 493–538 ISBN: 978-0-12-415845-0

P.J. Isaacson, C.M. Pieters, Decovolution of lunar olivine reflectance spectra: implications for remote compositional assessment. Icarus **210**, 8–13 (2010). doi:10.1016/j.icarus.2010.06.004

P.J. Isaacson, C.M. Pieters, S. Besse, R.N. Clark, J.W. Head, R.L. Klima, J.F. Mustard, N.E. Petro, M.I. Staid, J.M. Sunshine, L.A. Taylor, K.G. Thaisen, S. Tompkins, Remote compositional analysis of lunar olivine-rich lithogies with Moon Mineralogy Mapping(M^3) spectra. J. Geophys. Res. **116**, E00G11 (2011). doi:10.1029/2010JE003731

Y. Ishihara, S. Goossens, K. Matsumoto, H. Noda, H. Araki, N. Namiki, H. Hanada, T. Iwata, S. Tazawa, S. Sasaki, Crustal thickness of the Moon: implications for farside basin structures. Geophys. Res. Lett. **36**(19), L19202 (2009). doi:10.1029/2009GL039708

T. Iwata, N. Namiki, H. Hanada, H. Noda, N. Kawano, K. Matsumoto, S. Tsuruta, Q.H. Liu, F. Kikuchi, H. Minamino, T. Sasaki, Properties of SELENE small satellites for selenodetic measurements: Rstar(-OKINA) and Vstar(OUNA). Trans. Jpn. Soc. Aeronaut. Space Sci. Space Technol. Jpn. **7**, Tk_33–Tk_37 (2010). doi:10.2322/tstj.7.Tk_33

R. Jaumann, H. Hiesinger, M. Anand, I.A. Crawford, R. Wagner, F. Sohl, B.L. Jolliff, F. Scholten, M. Knapmeyer, H. Hoffmann, H. Hussmann, M. Crott, S. Hempel, U. Kohler, K. Krohn, N. Schmitz, J. Carpenter, M. Wieczorek, T. Spohn, M.S. Robinson, J. Oberst, Geology, geochemistry, and geophysics of the Moon: Status of current understanding. Planet. Space Sci. **74**, 15–41 (2012). doi:10.1016/j.pss.2012.08.019

B.L. Jolliff, J.J. Gillis, L.A. Haskin, R.L. Korotev, M.A. Wieczorek, Major lunar crustal terranes: surface expressions and crust-mantle origins. J. Geophys. Res. **105**(E2), 4197–4216 (2000). doi:10.1029/1999JE001103

B.L. Jolliff, M.A. Wieczorek, C.K. Shearer, C.R. Neal (eds.), *New Views of the Moon, Reviews in Mineralogy and Geochemistry*, vol. 60 (Mineralogical Society of America and Geochemical Society, DC, 2006), pp. 365–518 ISSN: 1529-6466

B.L. Jolliff, S.A. Wiseman, S.J. Lawrence, T.N. Tran, M.S. Robinson, H. Sato, B.R. Hawke, F. Scholten, J. Oberst, H. Hiesinger, C.H. van der Bogert, T. Greenhagen, T.D. Glotch, D.A. Paige, Compton–Belkovich: non-mare silicic volcanism on the Moon's far side. Nat. Geosci. **4**, 566–571 (2011). doi:10.1038/ngeo1212

B.L. Jolliff, M.A. Wieczorek, C.K. Shearer, C.R. Neal (eds.), *New Views of the Moon (in Chinese)*, (Geological Press House, 2012), ISBN: 0-939950-72-3

W.M. Kaula, *Theory of satellite geodesy* (Blaisdell, Waltham MA, 1966)

J.A.D. Khan, J. Connolly, J. Maclennan, K. Mosegaard, Joint inversion of seismic and gravity data for lunar composition and thermal state. Geophy. J. Int. **168**(1), 243–258 (2007). doi:10.1111/j.1365-246X.2006.03200.x

Khan, K. Mosegaard, An inquiry into the lunar interior: A non-linear inversion of the Apollo lunar seismic data. J. Geophys. Res. 107, E6, 5036, pp 3–1 ∼ 3–14(2002). doi:10.1029/2001JE001658

A. Khan, K. Mosegaard, K.L. Rasmussen, A new seismic velocity model for the Moon from a Monte Carlo inversion of the Apollo lunar seismic data. Geophys. Res. Lett. **27**(11), 1591–1594 (2000). doi:10.1029/1999GL008452

T. Kobayashi, H. Oya, T. Ono, A-scope analysis of subsurface radar sounding of lunar mare region. Earth Planets Space **54**, 973–982 (2002a)

T. Kobayashi, H. Oya, T. Ono, B-scan analysis of subsurface radar sounding of lunar highland region. Earth Planets Space **54**, 983–991 (2002b)

S. Kobayashi, N. Hasebe, E. Shibamura, O. Okudaira, M. Kobayashi, N. Yamashita, Y. Karouji, M. Hareyama, K. Hayatsu, S. Maurice, O. Gasnault, O. Forni, B. Diez, R.C. Reedy, K.J. Kim, Determining the absolute abundances of natural radioactive elements on the lunar surface by the Kaguya gamma-ray spectrometer. Space Sci. Rev. **154**, 193–218 (2010)

A.S. Konopliv, S.W. Asmar, E. Carramza, W.L. Sjogren, D.N. Yuan, Recent gravity models as a result of the Lunar Prosector mission. Icarus **150**, 1–18 (2001). doi:10.1006/icar.2000.6573

A.S. Konopliv, R.S. Park, D.-N. Yuan, S.W. Asmar, M.M. Watkins, J.G. Williams, E. Fahnestock, G. Kruizinga, M. Paik, D. Strekalov, N. Harvey, D.E. Smith, M.T. Zuber, The JPL lunar gravity field to spherical harmonic degree 660 from the GRAIL Primary Mission. J. Geophys. Res. **118**(7), 1415–1434 (2013). doi:10.1002/jgre.20097

R. Kovach, J. Watkins, P. Talwani, Active Seismic Experiement in Apollo 17 preliminary science report, NASA SP-330, p. 10–1 ∼ 10–12 (1973)

G.Y. Kramer, D.A. Kring, A.L. Nahm, C.M. Pieters, Spectral and photogeologic mapping of Schrödinger Basin and implications for post-South Pole-Aitken impact deep subsurface stratigraphy. Icarus **223**, 131–148 (2013). doi:10.1016/j.icarus.2012.11.008

Y.A. Kronrod, O.L. Kuskov, Inversion of seismic and gravity data for the composition and core sizes of the Moon. Phys. Solid Earth **47**(8), 711–730 (2011). doi:10.1134/S1069351311070044

B. Lafrance, B.E. John, J.S. Scoates, Syn-emplacement recrystalllization and deformation microstructures in the Poe Mountain anorthosite, Wyoming. Contrib. Mineral Petrol. **122**(4), 431–440 (1996). doi:10.1007/s004100050139

D.R. Lammlein, G.V. Latham, J. Dorman, Y. Nakamura, M. Ewing, Lunar seismicity, structures and tectonics. Rev. Geophys. **12**(1), 1–21 (1974). doi:10.1029/RG012i001p00001

M.L. Litvak, I.G. Mitrofanov, A. Sanin, A. Malakhov, W.V. Boynton, G. Chin, G. Droege, L.G. Evans, J. Gravin, D.V. Golovin, K. Harshman, T.P. McClanahan, M.I. Mokrousov, E. Mazarico, G. Milikh, G. Neumann, R. Sagdeev, D.E. Smith, R. Starr, M.T. Zuber, Global maps of lunar neutron fluxes from the LEND instrument. J. Geophys. Res. **117**, E00H22 (2012). doi:10.1029/2011JE00394

P.G. Lucey, B.R. Hawke, T.B. McCord, C.M. Pieters, J.W. Head, A compositional study of the Aristarchus region of the Moon using near-infrared reflectance spectroscopy. J. Geophys. Res. **91**(B4), D344–D354 (1986). doi:10.1029/JB091iB040D344

P.G. Lucey, Mineral maps of the Moon. Geophys. Res. Lett. **31**(8), L08701 (2004). doi:10.1029/2003GL019406

J.L. Margot, D.B. Campbell, R.F. Jurgens, M.A. Slade, Topography of the lunar poles from radar interferometry: a survey of cold trap locations. Science **284**(5420), 1658–1660 (1999). doi:10.1126/science.284.5420.1658

K. Matsumoto, S. Goossens, Y. Ishihara, Q. Liu, F. Kikuchi, T. Iwata, N. Namiki, H. Noda, H. Hanada, N. Kawano, F.G. Lemoine, D.D. Rowlands, An improved lunar gravity field model from SELENE and historical tracking data Revealing the farside gravity features. J. Geophys. Res. **115**(E6), E06007 (2010). doi:10.1029/2009JE003499

S. Maurice, D.J. Lawrence, W.C. Feldman, R.C. Elphic, O. Gasnault, Reduction of neutron data from Lunar Prospector. J. Geophys. Res. **109**(E7), E07S04 (2004). doi:10.1029/2003JE002208

E. Mazarico, F.G. Lemoine, S.-C. Han, D.E. Smith, GLGM-3: A degree-150 lunar gravity model from the historical gracking data of NASA Moon orbiters. J. Geophys. Res. **115**(E5), E05001 (2010). doi:10.1029/2009JE003472

E. Mazarico, G.A. Neumann, D.E. Smith, M.T. Zuber, M.H. Torrence, Illumination condition of the lunar polar regions using LOLA tography. Icarus. **211**, 1066–1081 (2011). doi:10.1016/j.icarus.2010.10.030

T.B. McCord, L.A. Taylor, J.P. Combe, G. Kramer, C.M. Pieters, J.M. Sunshine, R.N. Clark, Source and physical processes responsible for OH/H_2O in the lunar soil as revealed by the Moon Mineralogy Mapping(M^3). J. Geophys. Res. **116**, E00G05 (2011). doi:10.1029/2010JE003711

H.J. Melosh, A.M. Freed, B.C. Johnson, D.M. Blair, J.C. Andrews-Hann, G.A. Neumann, R.J. Phillips, D.E. Smith, S.C. Solomon, M.A. Wieczorek, M.T. Zuber, The origin of lunar mascon basins. Science **340**(6140), 1552–1555 (2013). doi:10.1126/science.1235768

I.G. Mitrofanov, A.B. Sanin, W.V. Boynton, G. Chin, J.B. Garvin, D. Golovin, L.G. Evans, K. Harshman, A.S. Kozyrev, M.L. Litvak, A. Malakhov, E. Mazarico, T. McClanahanm, G. Milikh, M. Mokrousov, G. Nandikotkur, G.A. Neumann, I. Nuzhdin, R. Sagdeev, V. Shevchenko, V. Shvetsov, D.E. Smith, R. Starr, V.I. Tretyakov, J. Trombka, D. Usikov, A. Varenikov, A. Vostrukhin, M.T. Zuber, Hydrogen mapping of the lunar south pole using the LRO Neutron detector experiment LEND. Science. **330**(6003), 483–486 (2010a). doi:10.1126/science.1185696

I.G. Mitrofanov, A. Bartels, Y.I. Bobrovnitsky, W. Boynton, G. Chin, H. Enos, L. Evans, S. Floyd, J. Garvin, D.V. Golovin, A.S. Grebennikov, K. Harshman, L.L. Kazakov, J. Keller, A.A. Konovalov, A.S. Kozyrev, A.R. Krylov, M.L. Litvak, A.V. Malakhov, T. McClanahan, G.M. Milikh, M.I. Mokrousov, S. Ponomareva, R.Z. Sagdeev, A.B. Sanin, V.V. Shevchenko, R. Starr, G.N. Timshenko, T.M. Tomilina, V.I. Tretyakov, J. Trombka, V.S. Troshin, V.N. Uvarov, A.B. Varennikov, A.A. Vostrukhin, Lunar exploration neutron detector for the NASA lunar reconnaissance orbiter. Space Sci. Rev. **150**(1–4), 183–207 (2010b). doi:10.1007/s112114-009-9608-4

I.G. Mitrofanov, M. Litvak, A. Sanin, A. Malakhov, D. Golovin, W. Boynton, G. Droege, G. Chin, L. Evans, K. Harshmann, F. Fedosov, J. Garvin, A. Kozyre, T. McClanahan, G. Milikh, M. Mokrousov, R. Star, R. Sagdeev, V. Shevchenko, V. Shvetsov, V. Tret'yakov, J. Trombka, A. Varenikv, A. Vostrukhin, Testing polar spots of water-rich permafrost on the Moon: LEND observation onboard LRO. J. Geophys. Res. **117**, E00H27 (2012). doi:10.1029/2011JE003956

P.M. Muller, W.L. Sjogren, Mascons: lunar mass concentrations. Science **161**(3842), 680–684 (1968). doi:10.1126/science.161.3824.680

J.F. Mustard, C.M. Pieters, P.J. Isaacson, J.W. Head, S. Besse, R.N. Clark, R.L. Klima, N.E. Petro, M.I. Staid, J.M. Sunshine, C.J. Runyon, S. Tompkins, Compositional diversity and geologic insights of the Aristarchus crater form Moon Mineralogy Mapping data. J. Geophys. Res. **116**, E000G12 (2011). doi:10.1029/2010JE003726

Y. Nakamura, Farside deep moonquakes and deep interior of the Moon. J. Geophys. Res. **110**, E01001 (2005). doi:10.1029/2004JE002332

Y. Nakamura, G.V. Latham, H.J. Dorman and J.E. Harris, UTIG Technical Report No. 18, revised version (2008)

Y. Nakamura, Seismology on the Moon—past, present and future. Ground-based geophysics on the Moon, #3005(2010)

N. Namiki, T. Iwata, K. Matsumoto, H. Hanada, H. Noda, S. Goossens, M. Ogawa, N. Kawano, K. Asari, S. Tsuruta, Y. Ishihara, Q. Liu, F. Kikuchi, T. Ishikawa, S. Sasaki, C. Aoshima, K. Kurosawa, S. Sugita, T. Takano, Farside Gravity field of the Moon from four-way Doppler measurements of SELENE(Kaguya). Science **323**(5916), 900–905 (2009). doi:10.1126/science.1168029

G.A. Neumann, M.T. Zuber, D.E. Smith, F.G. Lemoine, The lunar crust: global structure and signature of major basins. J. Geophys. Res. **101**(E7), 16841–16843 (1996). doi:10.1029/96JE01246

H. Noda, H. Araki, S. Goossens, Y. Ishihara, K. Matsumoto, S. Tazawa, N. Kawano, S. Sasaki, Illumination conditions at the lunar polar regions by KAGUYA(SELENE) laser altimeter. Geophys. Res. Lett. **35**(24), L24203 (2008). doi:10.1029/2008GL035692

S. Nozette, C.L. Lichtenberg, P. Spudis, R. Bonner, W. Ort, E. Malaret, M. Robinson, E.M. Shoemaker, The clementine bistatic radar experiment. Science **274**(5292), 1495–1498 (1996). doi:10.1126/science.274.5292.1495

S. Nozette, E.M. Shoemaker, P. Spudis, C.L. Lichtenberg, The possibility of ice on the Moon. Science **278**(5335), 144–145 (1997). doi:10.1126/science.278.5335.144

S. Nozette, P.D. Spudis, M.S. Robinson, B.J. Bussey, C. Lichtenberg, R. Bonner, Integration of lunar polar remote-sensing data sets: evidence for ice at the lunar south pole. J. Geophys. Res. **106**(E10), 23253–23266 (2001). doi:10.1029/2000JE001417

M. Ohtake, T. Matsunaga, J. Haruyama, Y. Yokata, T. Morota, C. Honda, Y. Ogawa, M. Torii, H. Miyamoto, T. Arai, N. Hirata, A. Iwasaki, R. Nakamura, T. Hiroi, T. Sugihara, H. Takeda, H. Otake, C.M. Pieters, K. Saiki, K. Kitazato, M. Abe, N. Asada, H. Demura, Y. Yamaguchi, S. Sasaki, S. Kodama, J. Terazono, M. Shirao, A. Yamaji, S. Minami, H. Akiyama, J.-L. Josset, The global distribution of pure anorthosite on the Moon. Nature. **461**, 236–240 (2009). doi:10.1038/nature08317

T. Ono, A. Kumamoto, H. Nakagawa, Y. Yamaguchi, S. Oshigami, A. Yamaji, T. Kobayashi, Y. Kasahara, H. Oya, Lunar radar sounder observation of subsurface layers under the nearside maria of Moon. Science **323**(5916), 909–912 (2009). doi:10.1126/science.1165988

T. Ono, A. Kumamoto, Y. Kasahara, Y. Yamaguchi, A. Yamaji, T. Kobayashi, S. Oshigami, H. Nakagawa, Y. Goto, K. Hashimoto, Y. Omura, T. Imachi, H. Matsumoto, H. Oya, The lunar radar sounder (LRS) onboard the Kaguya (SELENE) spacecraft. Space Sci. Rev. **154**, 145–192 (2010). doi:10.1007/s11214-010-9673-8

S. Oshigami, Y. Yamaguchi, A. Yamaji, T. Ono, A. Kumamoto, T. Kobayashi, H. Nakagawa, Distribution of the subsurface reflectors of the western nearside maria observed from Kaguya with lunar radar sounder. Geophys. Res. Lett. **36**(18), L18202 (2009). doi:10.1029/2009GL039835

D.A. Paige, M.A. Siegler, J.A. Zhang, P.O. Hayen, E.J. Foote, K.A. Bennett, A.R. Vasavada, B.T. Greenhagen, J.T. Schofield, D.J. McCleese, M.C. Foote, E. DeJong, B.G. Bills, W. Hartford, B.C. Murray, C.C. Allen, K. Snook, L.A. Soderblom, S. Calcut, F.W. Taylor, N.E. Bowles, J.L. Bandfield, R. Elphic, R. Ghent, T.D. Glotch, M.B. Wyatt, P.G. Lucey, Diviner lunar radiometer observations of cold traps in the Moon's south polar region. Science **330**(6003), 479–482 (2010). doi:10.1126/science.1187726

W.J. Peeples, W.R. Sill, T.W. May, S.H. Ward, R.J. Phillips, R.L. Jordan, E.A. Abbott, T.J. Killpack, Orbital radar evidence for lunar subsurface layering in Maria Serenitatis and Crisium. J. Geophys. Res. **83**(B7), 3459–3468 (1978). doi:10.1029/JB083iB07p03459

M. Pieters, Copernicus crater central peak: lunar mountain of unique composition. Science **215**(4528), 59–61 (1982). doi:10.1126/science.215.4528.59

C.M. Pieters, J.N. Goswami, R.N. Clark, M. Annadurai, J. Boardman, B. Buratti, J.-P. Combe, M.D. Dyar, R. Green, J.W. Head, C. Hibbitts, M. Hicks, P. Isaacson, R. Klima, G. Kramer, S. Kumar, E. Livo, S. Lundeen, E. Malaret, T. McCord, J. Mustard, J. Nettles, N. Petro, C. Runyon, M. Staid, J. Sunshine, L.A. Taylor, S. Tompkins, P. Varanasi, Character and spatial distribution of OH/H_2O on the surface of the Moon seen by M^3 on Chandrayaan-1. Science **326**(5952), 568–572 (2009). doi:10.1126/science.1178658

C.M. Pieters, S. Besse, J. Boardman, B. Buratti, L. Cheek, R.N. Clark, J.P. Combe, D. Dhingra, J.N. Goswami, R.O. Green, J.W. Head, P. Isaacson, R. Klima, G. Gramer, S. Lundeen, E. Malaret, T. McCord, J. Mustard, J. Nettles, N. Petro, C. Runyon, M. Staid, J. Sunshine, L.A. Taylor, K. Thaisen, S. Tompkins, J. Whitten, Mg-Spinel lithology: a new rock type on the lunar farside. J. Geophys. Res. **116**(E6), E00G08 (2011). doi:10.1029/2010JE003727

R.J. Phillips, G.F. Adams, W.E. Brown Jr, R.E. Eggleton, P.L. Jackson, R. Jordan, W.I. Linlor, W.J. Peeples, L.J. Porcello, J. Ryu, G. Schaber, W.R. Sill, T.W. Thompson, S.H. Ward, J.S. Zelenka, Apollo lunar sounder experiment. NASA Spec. Publ. **330**(22), 1–26 (1973a)

R.J. Phillips, G.F. Adams, W.E. Brown, Jr., R.E. Eggleton, P. Jackson, R. Jordan, W.J. Peeples, L.J. Porcello, J. Ryu, G. Schaber, W.R. Sill, T.W. Thompson, S.H. Ward, J.S. Zelenka, The Apollo 17 Lunar Souder, in *Proceedings of the 4th Lunar Science Conference*, 3, 2821–2831 (1973b)

A. Sanin, I.G. Mitrofanov, M. Litvak, A. Malakhov, W. Boynton, G. Droege, G. Chin, G. Droege, L. Evans, J. Garvin, D.V. Golovin, K. Harshmann, T.P. McClanahan, M.I. Mokrousov, E. Mazarico, G. Milikh, G. Neumann, R. Sagdeev, D.E. Smith, R.D. Starr, M.T. Zuber, Testing lunar permanently shadowed regions for water ice: LEND results from LRO. J. Geophys. Res. **117**, E00H26 (2012). doi:10.1029/2011JE003971

V.L. Sharpton, J.W. Head, Stratigraphy and Structural Evolution of Southern Mare Serenitatis: a Reinterpretation Based on Apollo Lunar Sounder Experiment Data. J. Geophys. Res. **87**(B13), 10983–10998 (1982). doi:10.1029/JB087iB13p10983

M.A. Siegler, B.G. Bills, D.A. Paige, Effects of orbital evolution on lunar ice stability. J. Geophys. Res. **116**(E3), E03010 (2011). doi:10.1029/2010JE003652

R.A. Simpson, G.L. Tyler, Reanalysis of Clementine bistatic radar data from the lunar South Pole. J. Geophys. Res. **104**(E2), 3845–3862 (1999). doi:10.1029/1998JE900038

R.B. Singer, Near-infrared spectral reflectance of mineral mixtures: systematic combinations of pyroxene, olivine, and iron oxides. J. Geophys. Res. **86**(B9), 7967–7982 (1981). doi:10.1029/JB086iB09p07967

D.E. Smith, M.T. Zuber, G.B. Jackson, J.F. Cavanaugh, G.A. Neumann, H. Riris, X. Sun, R.S. Zellar, C. Coltharp, J. Connelly, R.B. Katz, I. Kleyner, P. Liiva, A. Matuszeski, E.M. Mazarico, J.F. McGarry, A.-M. Novo-Gradac, M.N. Ott, C. Peters, L.A. Ramos-Izquierdo, L. Ramsey, D.D. Rowlands, S.

Schmidt, V.S. Scott III, G.B. Shaw, J.C. Smith, J.-P. Swinski, M.H. Torrence, G. Unger, A.W. Yu, T.W. Zagwodzki, The lunar orbiter laser altimeter investigation on the lunar reconnaissance orbiter mission. Space Sci. Rev. **150**, 209–241 (2010). doi:10.1007/s11214-009-9512-y

D. Spudis, S. Nozette, B. Bussey, K. Raney, H. Winters, C.L. Lichtenberg, W.M. Marinelli, J.C. Crusan, M.M. Gates, Mini-SAR: an imaging radar experiment for the Chandrayaan-1 mission to the Moon. Curr. Sci. **96**, 533–539 (2009)

P.D. Spudis, D.B.J. Bussey, S.M. Baloga, B.J. Butler, D. Carl, L.M. Carter, M. Chakraborty, R.C. Elphic, J.J. Gillis-Davis, J.N. Goswami, E. Heggy, M. Hillyard, R. Jensen, R.L. Kirk, D. LaVallee, P. McKerracher, C.D. Neish, S. Nozette, S. Nylund, M. Palsetia, W. Patterson, M.S. Robinson, R.K. Raney, R.C. Schulze, H. Sequeira, J. Skura, T.W. Whompson, B.J. Thomson, E.A. Ustinov, H.L. Winters, Initial results for the north pole of the Moon from Mini-SAR, Chandrayaan-1 mission. Geophys. Res. Lett. **37**(6), L06204 (2010). doi:10.1029/2009GL042259

P.D. Spudis, D.B.J. Bussey, S.M. Baloga, J.T.S. Cahill, L.S. Glaze, G.W. Patterson, R.K. Raney, T.W. Thompson, B.J. Thomson, E.A. Usinov, Evidence for water ice on the Moon: results for anomalous polar crater from the LRO Mini-RF imaging radar. J. Geophys. Res. Planets **118**(10), 2016–2029 (2013). doi:10.1002/jgre.20156

N.J. Stacy, D.B. Campbell, P.G. Ford, Arecibo radar mapping of the lunar poles: a search for ice deposits. Science **276**(5318), 1527–1530 (1997). doi:10.1126/science.276.5318.1527

J.M. Sunshine, T.L. Farnham, L.M. Feaga, O. Groussin, F. Merlin, R.E. Milliken, M.F. A'Hearn, Temporal and spatial variability of lunar hydration as observed by the deep impact spacecraft. Science **326**(5952), 565–568 (2009). doi:10.1126/science.1179788

S.R. Taylor, G.J. Taylor, L.A. Taylor, The Moon: a Taylor perspective. Geochim. Cosmochim. Acta **70**(24), 5904–5918 (2006). doi:10.1016/j.gca.2006.06.262

K.G. Thaisen, J.W. Head, L.A. Taylor, G.Y. Kramer, P. Isaacson, J. Nettles, N. Petro, C.M. Pieters, Geology of the Moscoviense Basin. J. Geophys. Res. **116**(E6), E00G07 (2011). doi:10.1029/2010JE003732

S. Tompkins, C.M. Pieters, Mineralogy of the lunar crust. Meteorit. Planet. Sci. **34**, 25–41 (1999). doi:10.1111/j.1945-5100.1999.tb01729.x

R. Vondrak, J. Keller, G. Chin, J. Garvin, Lunar Reconnaissance Orbitr (LRO): observations for Lunar Exploration and Science. Space Sci. Rev. **150**, 7–22 (2010). doi:10.1007/s11214-010-9631-5

W.R. Ward, Past orientation of the lunar spin axis. Science **189**(4200), 377–379 (1975). doi:10.1126/science.189.4200.377

R.C. Weber, Interior of the Moon, Chapter 24. *Encyclopedia of Solar System*, ed. by T. Spohn, T. Johnson, D. Breuer, 3rd edn. (Elsevier, Amsterdam, 2014), pp 539–554 ISBN: 978-0-12-415845-0

R.C. Weber, P.-Y. Lin, E.J. Garnero, Q. Williams, P. Lognonne, Seismic detection of the lunar core. Science **331**, 309–321 (2011). doi:10.1126/science.1199375

R.C. Weber, N.C. Schmerr, GRAIL refinements to lunar seismic structure, 45th Lunar and Planetary Science Conference, #2008(2014)

M.A. Wieczorek, R.J. Phillips, Potential anomalies on sphere: applications to the thickness of the lunar crust. J. Geophys. Res. **103**(E1), 1715–1724 (1998). doi:10.1029/97JE03136

M.A. Wieczorek, R.J. Phillips, The "Procellarum KREEP Terrane": implications for mare volcanism and lunar evolution. J. Geophys. Res. **105**(E8), 20417–20430 (2000). doi:10.1029/1999JE001092

M.A. Wieczorek, G.A. Neumann, F. Nimmo, W.S. Kiefer, G.J. Taylor, H.J. Melosh, R.J. Phillips, S.C. Solomon, J.C. Andrews-Hanna, S.W. Asmar, A.S. Konopliv, F.G. Lemoine, D.E. Smith, M.M. Watkins, J.G. Williams, M.T. Zuber, The crust of the Moon as seen by GRAIL. Science **339**(6120), 671–675 (2013). doi:10.1126/science.1231530

S. Yamamoto, R. Nakamura, R. Matsunaga, Y. Ogawa, Y. Ishihara, T. Morota, N. Hirata, M. Ohtake, T. Hiroi, Y. Yokota, J. Haruyama, Possible mantle origin of olivine around lunar impact basins detected by SELENE. Nat. Geosci. **3**, 533–536 (2010). doi:10.1038/ngeo897

S. Yamamoto, R. Nakamura, T. Matsunaga, Y. Ogawa, Y. Ishihara, T. Morota, N. Hirata, M. Ohtake, T. Hiroi, Y. Yokota, J. Haruyama, Olivine-rich exposures in the South Pole-Aitken Basin. Icarus **218**, 331–344 (2012). doi:10.1016/j.icarus.2011.12.012

N. Yamashita, N. Hasebe, R.C. Reedy, S. Kobayashi, Y. Karouji, M. Hareyama, E. Shibamura, M.-N. Kobayashi, O. Okudaira, C. d'Uston, O. Gasnault, O. Forni, K.J. Kim, Uranium on the Moon: global distribution and U/Th ratio. Geophys. Res. Lett. **37**(10), L10201 (2010). doi:10.1029/2010GL043061

M.T. Zuber, J.W. Head, G.A. Neumann, E. Mazarico, M.H. Torrence, O. Aharonson, A.R. Tye, C.I. Fasset, M.A. Rosenburg, H.J. Melosh, Constraints on the volatile distribution within Shackleton crater at the lunar south pole. Nat. Lett. **486**, 378–382 (2012). doi:10.1038/nature11216

M.T. Zuber, D.E. Smith, M.M. Watkins, S.W. Asmar, A.S. Konopliv, F.G. Lemoine, H.J. Melosh, G.A. Neumann, R.J. Phillips, S.C. Solomon, M.A. Wieczorek, J.G. Williams, S.J. Goossens, G. Kruizinga,

E. Mazarico, R.S. Park, D.-N. Yuan, Gravity field of the Moon from the gravity recovery and interior laboratory (GRAIL) mission. Science. **339**(6120), 668–671 (2013a). doi:10.1126/science.1231507

M.T. Zuber, D.E. Smith, D.H. Lehman, T.L. Hoffman, S.W. Asmar, M.M. Watkins, Gravity recovery and interior laboratory (GRAIL): mapping the lunar interior from crust to core. Space Sci. Rev. **178**, 3–24 (2013b). doi:10.1007/s11214-012-9952-7